

PERFORMANCE OF BILINEAR TIME-FREQUENCY TRANSFORMS IN ISAR

A THESIS SUBMITTED TO
THE GRADUATE SCHOOL OF NATURAL AND APPLIED SCIENCES
OF
MIDDLE EAST TECHNICAL UNIVERSITY

BY

BERKER LOĞOĞLU

IN PARTIAL FULFILLMENT OF THE REQUIREMENTS
FOR
THE DEGREE OF MASTER OF SCIENCE
IN
ELECTRICAL AND ELECTRONICS ENGINEERING

DECEMBER 2007

Approval of the thesis

**“PERFORMANCE OF BILINEAR TIME-FREQUENCY
TRANSFORMS IN ISAR”**

submitted by **Berker Loğođlu** in partial fulfillment of the requirements for the degree of **Master of Science in Electrical and Electronics Engineering** by,

Prof. Dr. Canan Özgen _____

Dean, **Graduate School of Natural and Applied Sciences**

Prof. Dr. İsmet Erkmen _____

Head of Department, **Electrical and Electronics Engineering**

Prof. Dr. Gülbin Dural _____

Supervisor, **EE, METU**

Examining Committee Members:

Assoc. Prof. Dr. Tolga Çilođlu _____

EE, METU

Prof. Dr. Gülbin Dural _____

EE, METU

Assoc. Prof. Dr. Şimşek Demir _____

EE, METU

Assoc. Prof. Dr. Sencer Koç _____

EE, METU

Prof. Dr. Feza Arıkan _____

EE, Hacettepe University

Date: _____

I hereby declare that all information in this document has been obtained and presented in accordance with academic rules and ethical conduct. I also declare that, as required by these rules and conduct, I have fully cited and referenced all material and results that are not original to this work.

Name, Last name : Berker Loğođlu

Signature :

ABSTRACT

PERFORMANCE OF BILINEAR TIME-FREQUENCY TRANSFORMS IN ISAR

Loğođlu, Berker

M.S., Department of Electrical and Electronics Engineering

Supervisor: Prof. Dr. Gülbin Dural

December 2007, 61 pages

In this thesis a stepped-frequency Inverse Synthetic Aperture Radar (ISAR) is employed to develop two-dimensional range-Doppler images of a small fighter aircraft which exhibits three dimensional rotational rotation. The simulation is designed such that the target can exhibit yaw, pitch and roll motions at the same time. First, radar returns from prominent scatterers of various parts of the target are processed and displayed using conventional Fourier transform. The effects of different complex motion types and scenarios are observed and discussed. Then, several linear and bi-linear time-frequency distributions including short-time Fourier transform, Wigner-Ville, pseudo Wigner-Ville, smoothed pseudo Wigner-Ville, Choi-Williams, Born-Jordan and Zhao-Atlas-Marks distributions are applied to the same target and scenarios. The performance of the transforms is compared for each scenario. The reasons for success of the distributions are discussed thoroughly.

Keywords: Inverse Synthetic Aperture Radar, Bilinear Time-Frequency Transforms

ÖZ

İKİ DOĞRUSAL ZAMAN-SIKLIK ÇEVİRİMİ İLE ISAR PERFORMANSI

Loğođlu, Berker

Yüksek Lisans, Elektrik-Elektronik Mühendisliđi Bölümü

Tez Yöneticisi: Prof. Dr. Gülbin Dural

Aralık 2007, 61 sayfa

Bu tezde aynı anda yalpa, alçalma-yükselme ve yuvarlanma hareketleri yapabilen bir hedefin ayrık-frekans Yapay Ağız Açıklıklı Radar ile görüntülenmesinin benzetimi yapılmıştır. İlk olarak geleneksel Fourier tabanlı yöntem ile farklı hareket senaryoları için menzil-Doppler görüntüsü elde edilmiştir. Elde edilen görüntüler değerlendirilmiş, sonuçlar sebepleri ile açıklanmıştır. Daha sonra aynı hedef ve senaryolara, geleneksel yöntem yerine zaman-frekans tabanlı doğrusal ve iki-doğrusal çevrimler uygulanmıştır. Uygulanan çevrimlerin performans karşılaştırmaları ve değerlendirmeleri yapılmış, başarı ve başarısızlık sebepleri irdelenmiştir. Uygulanan zaman-frekans yöntemleri sırası ile kısa-zaman Fourier çevrimi, Wigner-Ville, yalancı Wigner-Ville, yumuşatılmış yalancı Wigner-Ville, Choi-Williams, Born-Jordan ve Zhao-Atlas-Marks dağılımlarıdır.

Anahtar Kelimeler: Ters Yapay Ağız Açıklıklı Radar, İki Doğrusal Zaman-Sıklık Çevrimi

ACKNOWLEDGMENTS

I would like to thank to,

Prof. Dr. Gülbin Dural, my supervisor, for her steady support, encouragements and guidance along my education. Without her guidance and support, this thesis would not be possible,

Dr. Victor C. Chen, for his important simulation data about the work.

My parents, for their unlimited patience and for their constant supports.

TABLE OF CONTENTS

ABSTRACT	iv
ÖZ	v
ACKNOWLEDGMENTS	vi
TABLE OF CONTENTS	vii
LIST OF FIGURES	ix
CHAPTER	
1 INTRODUCTION	1
1.1 Radar Imaging	1
1.2 Related Work	2
1.3 Our Approach	2
1.4 Outline	4
2 INVERSE SYNTHETIC APERTURE RADAR IMAGING	5
2.1 Introduction	5
2.2 ISAR Theory	5
2.3 Stepped-Frequency ISAR	6
2.3.1 Introduction	6
2.3.2 Waveform	7
2.3.3 Quadrature Detection	8
2.3.4 Key Parameters	9
3 STEPPED-FREQUENCY ISAR SIMULATION WITH YAW,PITCH AND ROLL MOTIONS	12
3.1 Introduction	12
3.2 Manoeuvring Target Dynamics	12
3.3 Design Approach	17

3.4	Target Model	18
3.5	Radar Parameters	18
3.6	Simulation Results for Various Scenarios	19
3.7	Distortion Produced by Rotational Motion	21
3.7.1	Quadratic-Phase Distortion	22
3.7.2	Cell Migration	23
4	TIME-FREQUENCY TECHNIQUES IN ISAR	24
4.1	Introduction	24
4.2	Time-Frequency Image Formation	25
4.3	Linear Time-Frequency Transforms	27
4.3.1	Short-Time Fourier Transform	28
4.4	Bi-linear Time-Frequency Transforms	29
4.4.1	Wigner-Ville Distribution	32
4.4.2	Pseudo Wigner-Ville Distribution	33
4.4.3	Smoothed Pseudo Wigner-Ville Distribution	35
4.4.4	Choi-Williams Distribution	35
4.4.5	Born-Jordan Distribution	37
4.4.6	Zhao-Atlas-Marks Distribution	38
5	PERFORMANCE ANALYSIS OF TIME-FREQUENCY TRANSFORMS FOR VARIOUS COMPLEX MANOEUVRING TARGET SCENARIOS	41
5.1	Introduction	41
5.2	Scenario 1: Target with Yaw Motion	41
5.3	Scenario 2: Target with Yaw and Roll Motions	45
5.4	Scenario 3: Target with Yaw, Pitch and Roll Motions	49
5.5	Performance Analysis	54
6	CONCLUSIONS AND FUTURE WORK	56
	REFERENCES	58

LIST OF FIGURES

FIGURES

Figure 1.1	3D target rotation [11]	3
Figure 2.1	Range-Doppler image dimensions [22]	6
Figure 2.2	Stepped-Frequency ISAR image formation [10]	7
Figure 2.3	Quadrature Detector [36]	8
Figure 3.1	Geometry of the target [2]	13
Figure 3.2	Target image and the position of scatterers	18
Figure 3.3	Scenario 1: Conventional ISAR Image	20
Figure 3.4	Scenario 2: Conventional ISAR Image	20
Figure 3.5	Scenario 3: Conventional ISAR Image	21
Figure 4.1	Obtaining the time-range-Doppler cube by time-frequency based image formation [11]	26
Figure 4.2	Time-sampling in time-frequency based image formation [9]	26
Figure 4.3	Original ISAR image created by regular FFT approach	27
Figure 4.4	Images of simulated MIG-25 reconstructed by STFT using M/4 length windows.	29
Figure 4.5	Images of simulated MIG-25 reconstructed by STFT using M/32 length windows.	29
Figure 4.6	Images of simulated Boeing-727 reconstructed by STFT using M/4 length windows.	30
Figure 4.7	Images of simulated Boeing-727 reconstructed by STFT using M/32 length windows.	30
Figure 4.8	Images of simulated MIG-25 reconstructed using Wigner-Ville distribution	32

Figure 4.9 Images of simulated Boeing-727 reconstructed using Wigner-Ville distribution	33
Figure 4.10 Images of simulated MIG-25 reconstructed using pseudo Wigner-Ville distribution	34
Figure 4.11 Images of simulated Boeing-727 reconstructed using pseudo Wigner-Ville distribution	34
Figure 4.12 Images of simulated MIG-25 reconstructed using smoothed pseudo Wigner-Ville distribution	35
Figure 4.13 Images of simulated Boeing-727 reconstructed using smoothed pseudo Wigner-Ville distribution	36
Figure 4.14 Images of simulated MIG-25 reconstructed using Choi-Williams distribution	37
Figure 4.15 Images of simulated Boeing-727 reconstructed using Choi-Williams distribution	37
Figure 4.16 Images of simulated MIG-25 reconstructed using Born-Jordan distribution	38
Figure 4.17 Images of simulated Boeing-727 reconstructed using Born-Jordan distribution	38
Figure 4.18 Images of simulated MIG-25 reconstructed using Zhao-Atlas-Marks distribution	40
Figure 4.19 Images of simulated Boeing-727 reconstructed using Zhao-Atlas-Marks distribution	40
Figure 5.1 Scenario 1: Images reconstructed by STFT using $M/4$ length windows.	42
Figure 5.2 Scenario 1: Images reconstructed by STFT using $M/32$ length windows.	42
Figure 5.3 Scenario 1: Images reconstructed using Wigner-Ville distribution	43
Figure 5.4 Scenario 1: Images reconstructed using pseudo Wigner-Ville distribution	43
Figure 5.5 Scenario 1: Images reconstructed using smoothed pseudo Wigner-Ville distribution	43
Figure 5.6 Scenario 1: Images reconstructed using Choi-Williams distribution	44
Figure 5.7 Scenario 1: Images reconstructed using Born-Jordan distribution	44
Figure 5.8 Scenario 1: Images reconstructed using Zhao-Atlas-Marks distribution	45
Figure 5.9 Scenario 2: Images reconstructed by STFT using $M/4$ length windows.	46

Figure 5.10 Scenario 2: Images reconstructed by STFT using M/32 length windows.	46
Figure 5.11 Scenario 2: Images reconstructed using Wigner-Ville distribution . . .	46
Figure 5.12 Scenario 2: Images reconstructed using pseudo Wigner-Ville distribu- tion	47
Figure 5.13 Scenario 2: Images reconstructed using smoothed pseudo Wigner-Ville distribution	47
Figure 5.14 Scenario 2: Images reconstructed using Choi-Williams distribution . . .	48
Figure 5.15 Scenario 2: Images reconstructed using Born-Jordan distribution . . .	48
Figure 5.16 Scenario 2: Images reconstructed using Zhao-Atlas-Marks distribution	49
Figure 5.17 Scenario 3: Images reconstructed by STFT using M/4 length windows.	50
Figure 5.18 Scenario 3: Images reconstructed by STFT using M/32 length windows.	50
Figure 5.19 Scenario 3: Images reconstructed using Wigner-Ville distribution . . .	50
Figure 5.20 Scenario 3: Images reconstructed using pseudo Wigner-Ville distribu- tion	51
Figure 5.21 Scenario 3: Images reconstructed using smoothed pseudo Wigner-Ville distribution	51
Figure 5.22 Scenario 3: Images reconstructed using Choi-Williams distribution . . .	52
Figure 5.23 Scenario 3: Images reconstructed using Born-Jordan distribution . . .	52
Figure 5.24 Scenario 3: Images reconstructed using Zhao-Atlas-Marks distribution	53

CHAPTER 1

INTRODUCTION

1.1 Radar Imaging

Radar is an electromagnetic sensor that is widely used for detection, tracking and imaging of both stationary and moving objects such as aircraft, ships, ground vehicles. It is also used for generating high resolution maps of terrains. Radar sensors are superior to other type of sensors in the way that they can perform in all weather conditions at long distances with high accuracy [9]. Radar transmits electromagnetic waves and the radar receiver collects the returned signals from the scatterers of the object which are typically discontinuities, corners or cavities. The features of the object is described by the scattering properties of that object thus an image of the object can be constructed from the corresponding spatial distribution of the reflectivity. The image is usually mapped into down-range and cross-range planes. Down-range (slant-range) is the dimension along the line of sight (LOS) and cross-range is the perpendicular range to down-range [5]. To obtain high-resolution images is an important aspect. Resolution along down-range is determined by the radar's bandwidth and resolution along cross-range is determined by wavelength and viewing-angle segment. Thus, larger antenna aperture antenna must be used for higher cross-range resolution. To solve this problem, a synthetic aperture is utilized to emulate a large aperture antenna by coherently combining signals from sequences of small apertures [5]. Synthetic aperture radar (SAR) and inverse synthetic aperture radar (ISAR) are both synthetic array radars that emulate larger apertures.

SAR refers to the situation in which radar is moving whereas the target is stationary. It is an airborne or spaceborne radar mapping technique developed in the early 1950s that is used for generating high resolution maps of stationary surface targets and terrain. A SAR map is generated from reflectivity data collected as the radar passes the target area. ISAR

utilizes a geometrically inverse way of SAR. In ISAR, radar is stationary whereas the target is moving. It is used to image targets such as ships, aircraft and space objects. ISAR images are generated from reflectivity data collected from a single aperture as the target rotates [36].

1.2 Related Work

The ability to generate focused, high resolution images from ISAR systems is of great importance to military and intelligence operations. Thus, many works have been reported on high resolution ISAR imaging of moving airborne and naval targets [26], [31], [18], [27], [34]. One of the main challenges in ISAR image formation is the unknown nature of the target motion. So, removing the blurring and distortions using motion compensation has always been a challenge in ISAR concept [30], [29]. Various techniques are tried.

Different non time-frequency techniques are used in literature. Range instantaneous Doppler technique is implemented in [16]. An algorithm using the dechirp method is proposed in [1]. A super-resolution imaging method based on data extrapolation is carried out to enhance image resolution in [39]. Moving parameters of target is used to compensate the echo data in the two dimensional frequency space in [40]. The modified Doppler centroid tracking (MDCT) method which applies the phase gradient auto-focus (PGA) algorithm is used in [38]. To reduce the error of range alignment a minimum entropy criterion of range alignment in ISAR compensation is proposed in [17]. Range alignment using a minimum sum criterion is used in [35].

Besides from the mentioned techniques, time-frequency approach is the most common and the most successful one. Joint Time-Frequency Transforms are used in [23], [4], [5], [6], [7], [8], [9], [20], [21], [32], [33], [24].

1.3 Our Approach

In this thesis a stepped-frequency ISAR simulation is developed and various time-frequency techniques (TFTs) are applied for various scenarios. Developing an ISAR simulation and applying TFTs is not new in literature, many such work is done ([3], [11], [12]). Different from all those, in the developed ISAR simulation, the targets can exhibit not just two-dimensional (2D) rotation but all types of three-dimensional (3D) rotational movements; yaw, pitch and roll motions (see Figure 1.1). The simulation is implemented such that the

target can perform all three types of movements at the same time. Three different scenarios are implemented. In the first one is the target exhibits traditional simple rotation (yaw only), second one exhibits yaw and roll motions at the same time and the last one exhibits all three types of rotation at the same time.

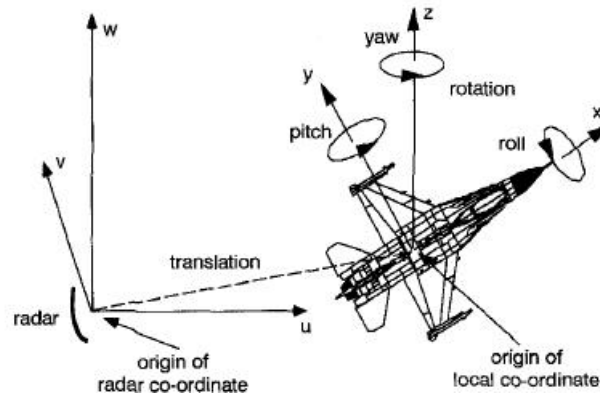


Figure 1.1: 3D target rotation [11]

As mentioned before, the time-frequency transforms are applied to ISAR in many past work ([4], [5], [6], [7], [8], [9], [20], [21], [32], [33]). However, the TFTs were applied to only simple 2D rotating targets. But in this thesis, various both linear and bi-linear time-frequency transforms including short-time Fourier transform, Wigner-Ville, pseudo Wigner-Ville, smoothed pseudo Wigner-Ville, Choi-Williams, Born-Jordan and Zhao-Atlas-Marks distributions to 3D rotating, complex manoeuvring targets. After all the transforms are applied and results are shown, ISAR image formation performance comparison for all the transforms is made and the results are discussed.

1.4 Outline

First of all, stepped-frequency ISAR is introduced, basic concepts and design parameters are explained in Chapter 2. Then, in Chapter 3, a stepped-frequency ISAR simulation with complex rotational motion is implemented. The target dynamics and the target model is explained. The chosen and calculated radar parameters used in the simulation are given and finally the images obtained by conventional Fourier transforms for various scenarios are shown. In Chapter 4, various linear and bi-linear time-frequency distributions are explained. Mathematical definitions are given and a basic discussion about their performance is made. Each distribution is applied to the simulated Mig-25 and Boeing-727 data provided by V.Chen [3]. In Chapter 5, the time-frequency distributions introduced in Chapter 4 are applied to the simulation scenarios implemented in Chapter 3. Performance of distributions for various complex manoeuvres are observed and the results are discussed. Finally, in Chapter 6 conclusions are given, results are evaluated and future work is discussed.

CHAPTER 2

INVERSE SYNTHETIC APERTURE RADAR IMAGING

2.1 Introduction

ISAR imaging systems are used to project the electromagnetic reflectivity properties of the targets reflective components such as wings, tail, nose, fuselage, engine and the weapons on to a two-dimensional plane. The dimensions of the ISAR image and the conversion of the targets electromagnetic reflectivity properties on to planar points have to be emphasized. The first image dimension becomes slant-range (the terms range or down-range are sometimes used interchangeably) to be question of imaging with ISAR systems. Range axis is the straight line which connects the target with the radar. The second image dimension is the cross-range (see Figure 2.1). Cross-range axis and equidistant cross-range lines lie perpendicular to the range axis. Because of the direct relation between the cross-range dimension and the Doppler information, the term range-Doppler imaging is also called instead of the term ISAR imaging in some sources [25].

2.2 ISAR Theory

The inverse synthetic aperture is formed by the coherent construction of signals obtained from the fixed aperture radar as the target translates and rotates within its beam-width, thus, creating the equivalent of a large circular aperture focused at the target's center-of-rotation (COR). The underlying idea in ISAR imaging is to use the Doppler information provided by the different velocities relative to the radar of those parts of the target characterized as individual scatterers to obtain high cross-range resolution. That is, the target is decomposed (spatially) into a set of individual point scatterers each of which has a different

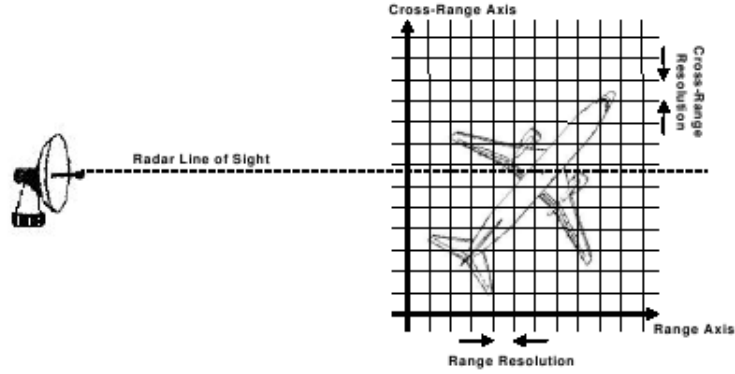


Figure 2.1: Range-Doppler image dimensions [22]

Doppler velocity represented by Doppler frequency shifts in the measured spectrum. Thus, the distribution of the target's reflectivity function can be measured by the Doppler spectrum. Typically, the Doppler spectrum is estimated using conventional Fourier transform techniques implemented computationally using the fast Fourier transform (FFT) algorithm with the underlying assumption that the Doppler frequency is fixed or time invariant. When the target moves this assumption is no longer valid and the Doppler spectrum is smeared degrading the cross-range resolution.

2.3 Stepped-Frequency ISAR

2.3.1 Introduction

Stepped-frequency (SF) modulated radar is selected in our applications for its high range resolution. It employs inter-pulse compression, in which the carrier frequency of successive pulses is changed by a fixed frequency step, Δf . Due to this technique, a wide bandwidth is inherently achieved over several pulses instead of within a single pulse. The product of the number of coherently integrated pulses, N , and the frequency step size gives the effective stepped-frequency waveform (SFWF) bandwidth.

High resolution range (HRR) profile is obtained by taking the inverse fast Fourier transform (IFFT) of the frequency spectrum of the target reflectivity which is formed by the returns of the N pulses at different carrier frequencies. HRR profile gives the relative position of each scatterer. Detailed stepped-frequency ISAR formation steps are shown in Figure 2.2. Throughout this chapter, only detailed explanations on key subjects about stepped-frequency ISAR which are used in the simulation developed in Chapter 3 are made.

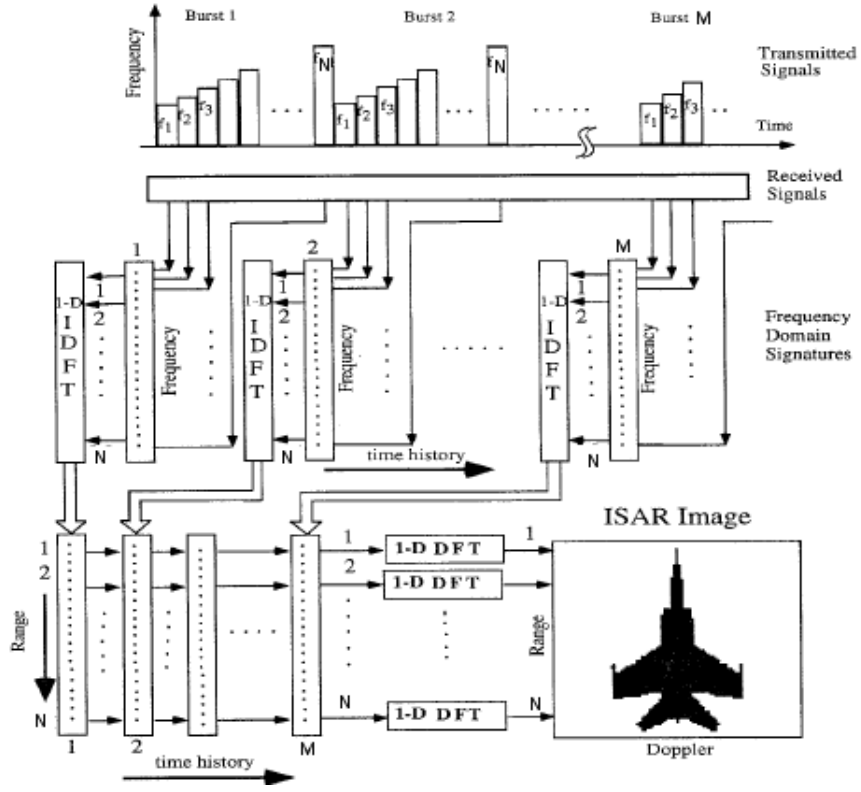


Figure 2.2: Stepped-Frequency ISAR image formation [10]

2.3.2 Waveform

The stepped-frequency radar transmits a sequence of N pulses at a fixed pulse repetition frequency (PRF). Each set of pulses is called a burst or a coherent processing interval. Each pulse in a sequence is transmitted with a different carrier frequency. The frequency is linearly increased from pulse to pulse by a fixed increment Δf . The carrier frequency for the n -th pulse can be written as:

$$f_n = f_0 + n\Delta f \quad (2.1)$$

where f_0 is the nominal carrier frequency and Δf is the frequency step size. Thus the transmitted signal for the n -th pulse can be written as:

$$s_T = A_T \cos[2\pi(f_0 + n\Delta f)t] \quad (2.2)$$

where A_T is the amplitude of the transmitted signal. Thus the transmitted signal is:

$$s_R = A_R \cos[2\pi(f_0 + n\Delta f)(t - \frac{2R}{c})] \quad (2.3)$$

where $\frac{2R}{c}$ is the delay time of the signal, A_R is the attenuated signal amplitude and c is the speed of light.

2.3.3 Quadrature Detection

Phase information and the Doppler shift is one of the most important steps of ISAR. Quadrature detection is used to retrieve phase information relative to the transmitted signal. It is also called coherent phase detector and is illustrated in Figure 2.3.

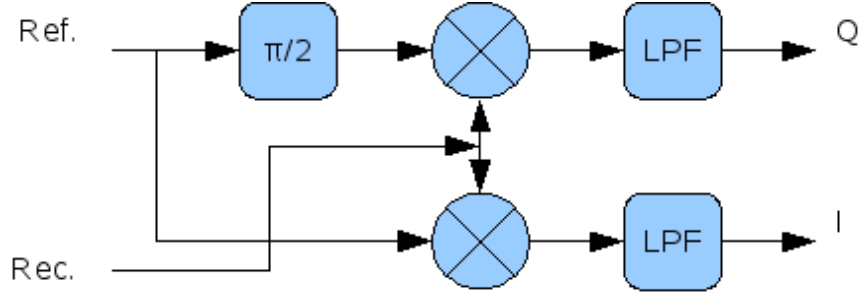


Figure 2.3: Quadrature Detector [36]

$$\begin{aligned} s_{R_I}(t) &= LPF\{A_T A_R \cos[2\pi(f_0 + n\Delta f)t] \cos[2\pi(f_0 + n\Delta f)(t - \frac{2R}{c})]\} \\ &= LPF\{\frac{A_T A_R}{2} \{\cos[2\pi(f_0 + n\Delta f)t - 2\pi(f_0 + n\Delta f)(t - \frac{2R}{c})] + \cos[2\pi(f_0 + n\Delta f)\frac{2R}{c}]\}\} \end{aligned} \quad (2.4)$$

$$s_{R_Q}(t) = LPF\{A_T A_R \sin[2\pi(f_0 + n\Delta f)t] \cos[2\pi(f_0 + n\Delta f)(t - \frac{2R}{c})]\} \quad (2.5)$$

where $s_{R_I}(t)$ is the in-phase (I) and $s_{R_Q}(t)$ is the quadrature (Q) output of the received signal s_R after the mixing operation. It should be noted that the high frequency terms will

be filtered out by the low pass filter (LPF). Then, the output of the quadrature detector can be written as:

$$s_{Raw}(t) = s_{R_I}(t) + js_{R_Q}(t) = Ae^{-j\phi_n} \quad (2.6)$$

where:

$$\phi_n = 2\pi(f_0 + n\Delta f)\frac{2R}{c} \quad (2.7)$$

If the target moves with a constant radial velocity v_R , then the range must be represented as:

$$R_n = R_0 + nv_RT \quad (2.8)$$

where T is the pulse repetition interval (PRI). Thus, the phase can be represented as:

$$\phi_n = \frac{4\pi f_0 R_0}{c} + \frac{4\pi \Delta f R_0 (n-1)T}{c} + \frac{4\pi f_0 (n-1)T}{c} + \frac{4\pi \Delta f v_R (n-1)^2 T^2}{Tc} \quad (2.9)$$

2.3.4 Key Parameters

In a stepped-frequency radar design the calculations of the following parameters must be well known and carefully chosen to satisfy the design parameters such as bandwidth, down-range and cross-range resolutions:

Bandwidth

The instantaneous bandwidth of a stepped-frequency radar system is same as a single pulse system:

$$B_{inst} = \frac{1}{\tau} \quad (2.10)$$

where τ is the pulse width. But the effective bandwidth is:

$$B_{eff} = N\Delta f \quad (2.11)$$

A stepped-frequency radar system is designed such that:

$$B_{eff} > B_{inst} \quad (2.12)$$

Range Resolution

The range (down-range) resolution of a conventional radar is given as:

$$\Delta r_d = \frac{c\tau}{2} \quad (2.13)$$

Compared to conventional systems, much smaller range resolution values can be obtained:

$$\Delta r_{d,step} = \frac{c}{2B_{eff}} = \frac{c}{2N\Delta f} = \frac{R_u}{N} \quad (2.14)$$

where R_u is the unambiguous range window [36]. As seen from 2.14, increasing the number of pulses or increasing the frequency step size ends up with smaller range resolution values.

To prevent range ambiguities, R_u must be chosen larger than the maximum target extent (E):

$$R_u = \frac{c}{N\Delta f} \geq E \implies \Delta f \leq \frac{c}{2E} \quad (2.15)$$

Cross-range Resolution

Assume a target with all scatterers on the same horizontal plane rotates with a constant angular rotation speed of w rad/s about the axis that is perpendicular to the horizontal plane.

For a scatterer at a cross-range distance of r_c from the center of rotation, the instantaneous tangential velocity towards radar will be wr_c , thus, the corresponding instantaneous Doppler frequency shift will be:

$$f_d = 2wr_c \frac{f_c}{c} \quad (2.16)$$

where f_c is the carrier frequency. For two scatterers located in the same down-range that are separated in the cross-range by Δr_c , the frequency difference is computed as:

$$\Delta f_d = 2w\Delta r_c \frac{f_c}{c} \quad (2.17)$$

The Doppler resolution is approximately given by:

$$\Delta f_d = \frac{1}{T} \quad (2.18)$$

where T is the coherent integration (total observation) time. Thus, for a Doppler resolution of Δf_d the corresponding cross-range resolution is calculated as [36]:

$$\Delta r_c = \frac{c\Delta f_d}{2wf_c} = \frac{c}{2wT_i f_c} \quad (2.19)$$

CHAPTER 3

STEPPED-FREQUENCY ISAR SIMULATION WITH YAW,PITCH AND ROLL MOTIONS

3.1 Introduction

Both real and simulated ISAR data is very hard to obtain. The only simulated ISAR data that could be obtained from [3] in which the target exhibits simple 2D rotation is processed in Chapter 4. However, this data is not sufficient since the performance of time-frequency transforms for complex manoeuvring targets is wanted to be examined. For further investigation, because of the lack of data, a stepped-frequency ISAR simulation in which the target is capable of having 3D rotational motions which consists yaw, pitch and roll motions rather than just 2D rotation is implemented.

Throughout this chapter, since it is the key point, manoeuvring target dynamics will be explained first [12], [11]. Then, the key parameters which are explained in Chapter 2 will be selected and calculated, the target model will be defined, design approach will be explained step by step and the ISAR simulation results for three different scenarios to be defined will be shown.

3.2 Manoeuvring Target Dynamics

A manoeuvring target is defined as a target that has possibly nonuniform translational and rotational motion during the observation time. For simplicity, let's define a planar target in 2D Cartesian coordinates (x,y,z) . The geometric center is defined at the origin of the Cartesian coordinate system. The radar is defined to be located at the origin or

another Cartesian coordinate system (u,v,w) . Two different coordinate systems are defined to describe the rotation of the target properly (see Figure 3.1).

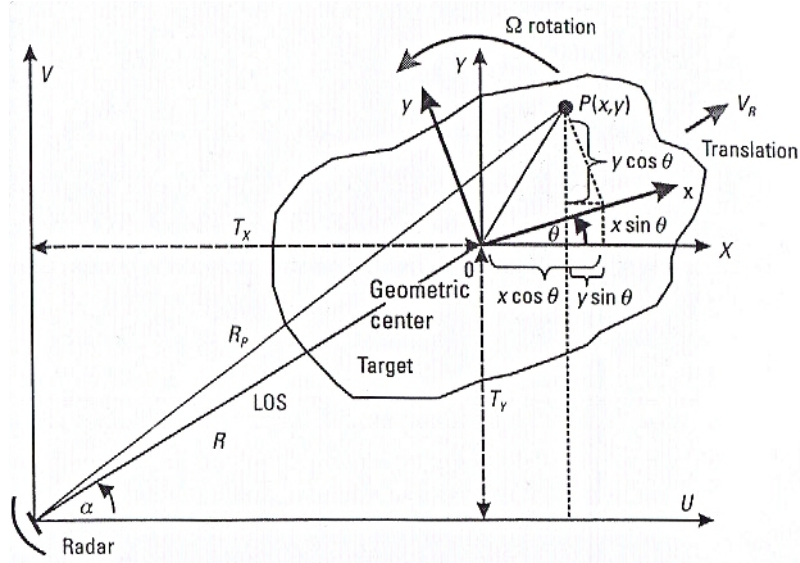


Figure 3.1: Geometry of the target [2]

R is the distance from the geometric center of the target to the radar, where R_p is the distance from the point scatterer P . θ_0 is the initial rotational angle about the z -axis and α is the azimuth angle of the target with respect to the radar coordinate system. Then, R_p is calculated as [2]:

$$\begin{aligned}
 R_p &= [(T_x + x \cos \theta_0 - y \sin \theta_0)^2 + (T_y + y \cos \theta_0 + x \sin \theta_0)^2]^{1/2} \\
 &= \{R^2 + (x^2 + y^2) + 2R[x \cos(\theta_0 - \alpha) - y \sin(\theta_0 - \alpha)]\}^{1/2} \\
 &\simeq R + x \cos(\theta_0 - \alpha) - y \sin(\theta_0 - \alpha)
 \end{aligned} \tag{3.1}$$

This is the case when the origin of the target is assumed to be stationary, i.e. $(T_x, T_y, T_z = 0)$. Let's assume the target has translational motion as well as rotational motion only in the x - y plane where v_R is the initial radial velocity and its constant. The orientation of the target changes during the observation time $\Delta t = t - t_0$. Assume $R \gg R - R_p$ so that neglect the change in α and assume its constant. Then [2]:

$$\begin{aligned}
R_p(t) &= R(t) + x \cos(\theta_t - \alpha) - y \sin(\theta_t - \alpha) \\
R(t) &= R_0 + v_R t \\
\theta_t &= \theta_0 + \Omega t
\end{aligned} \tag{3.2}$$

where Ω is the angular rotation rate. Then the phase of the returned signal from the scatterer is calculated as [2]:

$$\phi(R_p(t)) = 2\pi f_0 \frac{2R_p(t)}{c} \tag{3.3}$$

where c is the speed of electromagnetic wave propagation in air. By taking the time-derivative of the phase function the induced Doppler frequency shift can be derived as [2]:

$$\begin{aligned}
f_D &= \frac{2f_0}{c} \frac{d}{dt} R_p(t) \\
&= \frac{2f_0}{c} v_R + \frac{2f_0}{c} \{-x\Omega[\sin(\theta_0 - \alpha) \cos \Omega t + \cos(\theta_0 - \alpha) \sin \Omega t] \\
&\quad - y\Omega[\cos(\theta_0 - \alpha) \cos \Omega t + \sin(\theta_0 - \alpha) \sin \Omega t]\} \\
&\simeq \frac{2f_0}{c} v_R + \frac{2f_0}{c} \{-[x \sin[\theta_0 - \alpha] + y \cos(\theta_0 - \alpha)]\Omega \\
&\quad - [x \cos[\theta_0 - \alpha] - y \sin(\theta_0 - \alpha)]\Omega^2 t\}
\end{aligned} \tag{3.4}$$

Then translation motion induced Doppler frequency is:

$$f_{D_{Trans}} = \frac{2f_0}{c} v_R \tag{3.5}$$

and the rotational motion induced Doppler frequency is :

$$f_{D_{Rot}} = \frac{2f_0}{c} \{-[x \sin[\theta_0 - \alpha] + y \cos(\theta_0 - \alpha)]\Omega - [x \cos[\theta_0 - \alpha] - y \sin(\theta_0 - \alpha)]\Omega^2 t\} \tag{3.6}$$

Roll, pitch and yaw are the frequently used set of rotational motions. These motions are shown in Figure 1.1. For a target heading along the x-axis, the target's coordinates can be written by the following matrices:

$$Roll(x, \theta_r) = \begin{bmatrix} 1 & 0 & 0 & 0 \\ 0 & \cos \theta_r & -\sin \theta_r & 0 \\ 0 & \sin \theta_r & \cos \theta_r & 0 \\ 0 & 0 & 0 & 1 \end{bmatrix} \quad (3.7)$$

$$Pitch(y, \theta_p) = \begin{bmatrix} \cos \theta_p & 0 & \sin \theta_p & 0 \\ 0 & 1 & 0 & 0 \\ -\sin \theta_p & 0 & \cos \theta_p & 0 \\ 0 & 0 & 0 & 1 \end{bmatrix} \quad (3.8)$$

$$Yaw(z, \theta_y) = \begin{bmatrix} \cos \theta_y & -\sin \theta_y & 0 & 0 \\ \sin \theta_y & \cos \theta_y & 0 & 0 \\ 0 & 0 & 1 & 0 \\ 0 & 0 & 0 & 1 \end{bmatrix} \quad (3.9)$$

$$Rot(\theta_r, \theta_p, \theta_y) = \begin{bmatrix} a_{11} & a_{12} & a_{13} & 0 \\ a_{21} & a_{22} & a_{23} & 0 \\ a_{31} & a_{32} & a_{33} & 0 \\ 0 & 0 & 0 & 1 \end{bmatrix} \quad (3.10)$$

where:

$$\begin{aligned}
a_{11} &= \cos \theta_p \cos \theta_y \\
a_{12} &= -\cos \theta_p \sin \theta_y \\
a_{13} &= \sin \theta_p \\
a_{21} &= \sin \theta_r \sin \theta_p \cos \theta_y + \cos \theta_r \sin \theta_y \\
a_{22} &= -\sin \theta_r \sin \theta_p \sin \theta_y + \cos \theta_r \cos \theta_y \\
a_{23} &= -\sin \theta_r \cos \theta_p \\
a_{31} &= -\cos \theta_r \sin \theta_p \cos \theta_y + \sin \theta_r \sin \theta_y \\
a_{32} &= \cos \theta_r \sin \theta_p \sin \theta_y + \sin \theta_r \cos \theta_y \\
a_{33} &= \cos \theta_r \cos \theta_p
\end{aligned} \tag{3.11}$$

Composite translational and rotational motion can be presented by the following matrix:

$$Trans(T_x, T_y, T_z) Rot(\theta_r, \theta_p, \theta_y) = \begin{bmatrix} a_{11} & a_{12} & a_{13} & T_x \\ a_{21} & a_{22} & a_{23} & T_y \\ a_{31} & a_{32} & a_{33} & T_z \\ 0 & 0 & 0 & 1 \end{bmatrix} \tag{3.12}$$

Thus, the coordinates of any manoeuvring target can be calculated by:

$$\begin{bmatrix} x_t \\ y_t \\ z_t \\ 1 \end{bmatrix} = \begin{bmatrix} a_{11} & a_{12} & a_{13} & T_x \\ a_{21} & a_{22} & a_{23} & T_y \\ a_{31} & a_{32} & a_{33} & T_z \\ 0 & 0 & 0 & 1 \end{bmatrix} \begin{bmatrix} x_0 \\ y_0 \\ z_0 \\ 1 \end{bmatrix} \tag{3.13}$$

3.3 Design Approach

To simplify the design, some important assumptions are done before starting:

- All scatterers are assumed to have same radar cross section.
- No multiple scattering mechanisms are considered.
- Scatterers do not shadow each other.
- Location of scatterers change only from one burst to another.
- The coordinate axes of the radar and the target are aligned.
- Translational motion is compensated.

After the assumptions are done, the following steps are followed in the simulation:

- Radar parameters are selected, locations of radar scatterers are defined.
- Doppler velocity for each scatterer at each burst is determined.
 - Initial center to radar, scatterer to center and scatterer to radar vectors are calculated.
 - Initial yaw, pitch, roll angles are calculated using the vectors calculated in the previous step.
 - Change of angles for each burst for each scatterer are calculated according to rotation rates.
 - New position of each scatterer is calculated for each burst according to equation 3.13.
 - Doppler velocities are calculated using the velocity and position information of individual scatterer positions, thus target returns for each scatterer for each burst are calculated.
- In-phase and quadrature-phase components are calculated, these components are processed using IFFT.
- Doppler profile is generated using FFT.
- Range-Doppler image is created.

3.4 Target Model

A jet fighter aircraft like an F-16 is tried to be simulated. Thus, the length and wingspan of the aircraft are chosen as 15 m and 12 m respectively. The aircraft is modeled with 22 scatterer points. The 2D and 3D positions of scatterers are shown in Figure 3.2. Point scatterer model is chosen since:

- It is simple to implement
- Image formation algorithms are easily compared.
- Target's motion is easy to simulate and effect of rotational motions are clearly observed.

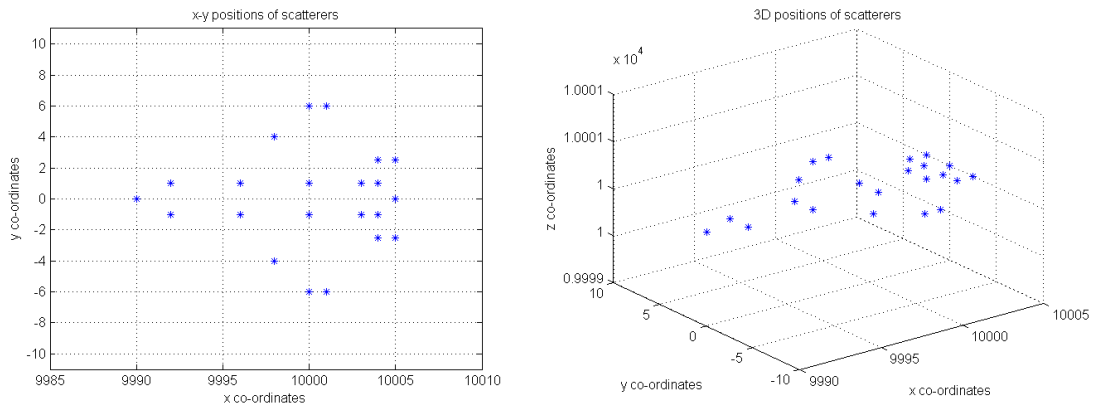


Figure 3.2: Target image and the position of scatterers

3.5 Radar Parameters

A range resolution of 0.3 m and a cross-range resolution of 0.1 m is wanted to be achieved. No range ambiguity is wanted. So using the equations defined in section 2.3.4, the following radar parameters are selected and calculated:

- Carrier frequency: 9 GHz
- Pulse repetition frequency: 15 kHz
- Stepped frequency step size: 8 MHz

- Number of stepped frequency steps: 64
- Number of burst for ISAR processing: 512
- Effective bandwidth: 512 MHz
- Total observation time: 2.18 s
- Range resolution: 0.29 m
- Cross-range resolution (for $w=0.2$ rad/s): 0.095 m

3.6 Simulation Results for Various Scenarios

Different manoeuvres are simulated in the following three scenarios. All the motions and rotation rates defined are within the limits of a fighter aircraft. Since none of the rotational motion compensation algorithms is not applied, all the obtained images are blurred due to fast rotation and relatively long observation time (see Figure 3.3, Figure 3.4, and Figure 3.5). It is impossible to resolve the scattering points. It should be noted that the distortion is caused only by rotational motion since translational motion is assumed to be perfectly compensated. The causes of the distortion will be further investigated in section 3.7 after all the results are shown.

These scenarios will further be processed by time-frequency transforms, and higher resolution images will be tried to be formed in Chapter 5.

Scenario 1

The first scenario is the one that exhibits the simplest motion. The target is defined to have only yaw motion similar to the ones in [3]. The yaw rate is defined as 0.15 rad/s. Definition of yaw, pitch and roll motions for our target model defined in Section 3.4 can be seen in Figure 1.1. Simulated range-Doppler image is shown in Figure 3.3.

Scenario 2

The second scenario is more complex. The target is defined to have 0.1 rad/s yaw and 0.25 rad/s roll motions. Simulated range-Doppler image is shown in Figure 3.4.

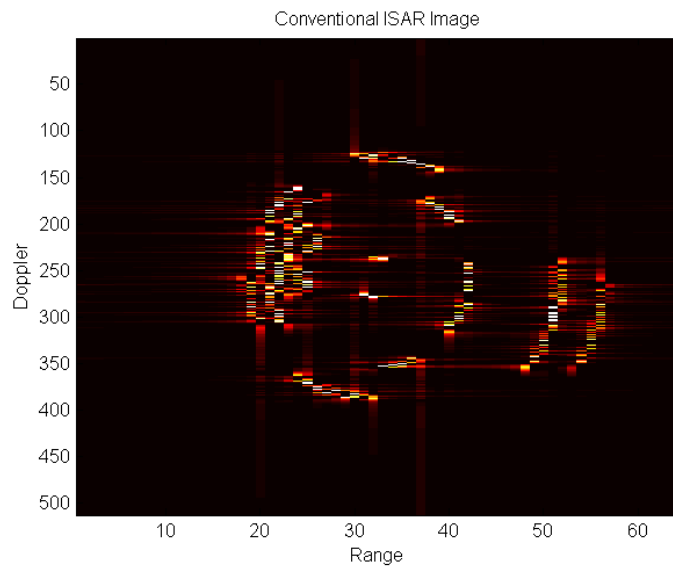


Figure 3.3: Scenario 1: Conventional ISAR Image

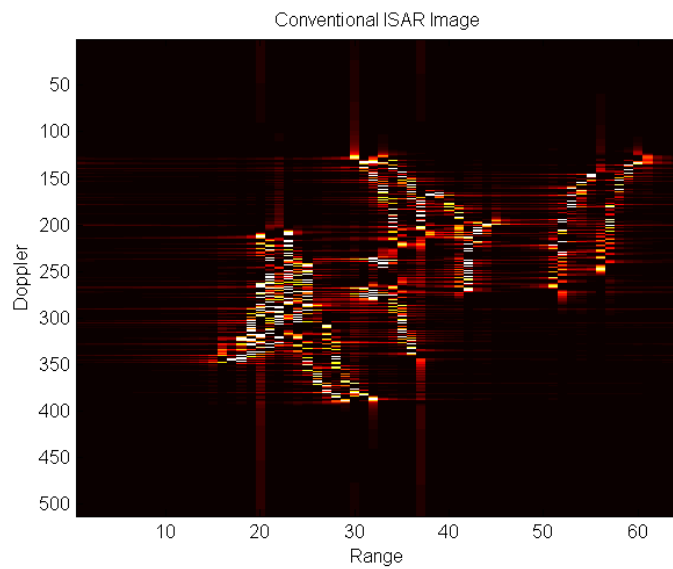


Figure 3.4: Scenario 2: Conventional ISAR Image

Scenario 3

The third scenario is the most complex one. The target is defined to have 0.1 rad/s yaw, 0.1 rad/s pitch and 0.2 rad/s roll motions at the same time. Simulated range-Doppler image is shown in Figure 3.5.

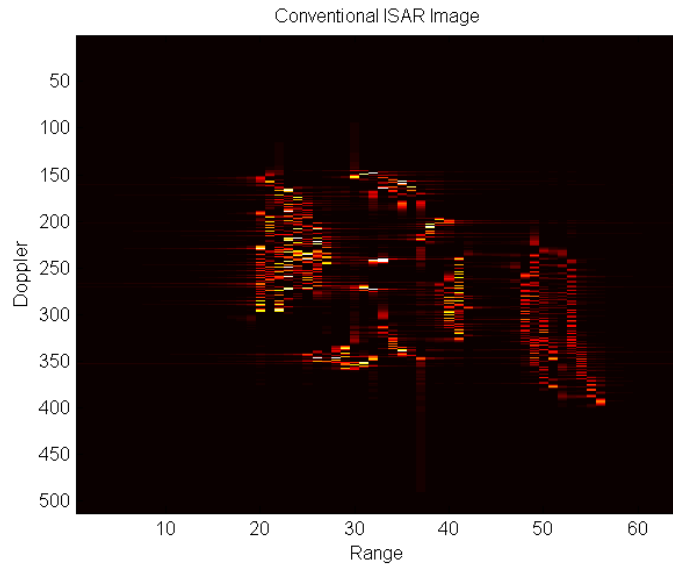


Figure 3.5: Scenario 3: Conventional ISAR Image

3.7 Distortion Produced by Rotational Motion

Cross-range resolution is achieved by Doppler gradient which is produced by target rotation. However, the same rotation is also the cause of distortion. The velocity components of target's individual back-scattering centers toward the radar are not constant since their motion relative to target's rotational axis is circular. These back-scattering centers follow curved paths. Thus, generating range profiles by applying IFFT for each range cell results in nonlinear phase slope which causes a distorted image [36].

The effect of nonlinear phase slope will be analyzed in terms quadratic-phase distortion and distortion produced by cell migration [36]. Since the distortion is independent of the method used for range profile generation, distortion will be analyzed in terms of real range profiles for simplicity.

3.7.1 Quadratic-Phase Distortion

Assuming a single scatterer at radius r from the target's rotation axis, rotating with w rad/s and the distance from radar to the rotation axis is R , range delay to the scatterer becomes:

$$\tau(t) = \frac{2R}{c} - \frac{2r}{c} \cos(wt - \theta) \quad (3.14)$$

Phase associated with $\tau(t)$ is:

$$\phi(t) = -2\pi f_0 \tau(t) = -2\pi f_0 \left\{ \frac{2R}{c} - \frac{2r}{c} \cos(wt - \theta) \right\} \quad (3.15)$$

The Doppler frequency shift produced is:

$$f_d(t) = \frac{1}{2\pi} \frac{d\phi(t)}{dt} = -f_0 \frac{2wr}{c} \sin(wt - \theta) \quad (3.16)$$

Assuming $\theta = 0$, for small wt the phase response can be written as:

$$\begin{aligned} \phi(t) &\simeq -2\pi f_0 \left\{ \frac{2R}{c} - \frac{2r}{c} \left(1 - \frac{(wt)^2}{2!} \right) \right\} \\ \phi(t) &= -\frac{4\pi R}{\lambda} + \frac{4\pi r}{\lambda} - \frac{4\pi}{\lambda} \frac{v^2 t^2}{2r} \end{aligned} \quad (3.17)$$

where v is the cross-range velocity. The first two terms represents the total phase advance to the scatterer at $t = 0$ whereas the third term is the quadratic-phase term which produces the distortion [36].

3.7.2 Cell Migration

Cell migration is the movement of scatterers across range cells. It occurs when the scatterers shift at least one resolution cell because of large data integration angle wT . The movement across range cells can occur in both down-range and cross-range dimensions. Both migration types blur the ISAR image.

For the same scatterer described in section 3.7.1, the down-range between the radar and the scatterer is $R - r\cos(wt - \theta)$. During target rotation, the change in down-range is maximum at the cross-range extremes when $\theta = \pi/2$. Thus the number of down-range resolution cells that the scatterer will migrate during the observation time T is given as [36]:

$$\begin{aligned} M_d &= \left| \frac{1}{\Delta r_d} \{ [R - r\cos(wt - \frac{\pi}{2})]_{t=0} - [R - r\cos(wt - \frac{\pi}{2})]_{t=T} \} \right| \\ M_d &= \left| \frac{r\sin(wT)}{\Delta r_d} \right| \end{aligned} \quad (3.18)$$

where Δr_d is the down-range resolution.

Similarly, during target rotation, the change in cross-range is maximum at the down-range extremes when $\theta = 0/2$. Thus the number of cross-range resolution cells that the scatterer will migrate during the observation time T is given as [36]:

$$M_c = \left| \frac{1}{\Delta f_d} (f_d|_{t=0} - f_d|_{t=T}) \right| \quad (3.19)$$

Using Equation (3.16), for Doppler resolution given by $1/T$, we obtain:

$$M_c = \left| \frac{2f_0rwT}{c} \sin(wT) \right| \quad (3.20)$$

CHAPTER 4

TIME-FREQUENCY TECHNIQUES IN ISAR

4.1 Introduction

In this chapter, time-frequency image formation and various time-frequency transforms (TFT) that will be compared are thoroughly explained. Before defining any time-frequency transform, the Fourier transform $S(w)$ of a signal must be defined. The Fourier transform $S(w)$ of a time signal $s(t)$ is defined as:

$$S(w) = \int_{-\infty}^{\infty} s(t) e^{-j\omega t} dt \quad (4.1)$$

The inverse Fourier transform is defined as:

$$s(t) = \frac{1}{2\pi} \int_{-\infty}^{\infty} S(w) e^{-j\omega t} d\omega \quad (4.2)$$

One of the most known and important property of the Fourier transform pair $s(t)$ - $S(w)$ is the uncertainty principle whose importance will be discussed in Section 4.3.1 when discussing short-time Fourier transform:

$$\Delta_t \Delta_w \geq \frac{1}{2} \quad (4.3)$$

where Δ_t is the time duration of $s(t)$ and Δ_w is the frequency bandwidth of $S(w)$.

Characterization of the time-varying frequency content of a signal is the basic idea of time-frequency analysis. It is used when frequency content of the signal of interest change over time and tracking this change is important. It has applications in acoustic analysis, radar tracking, and speech processing. Using such an analysis in ISAR, highly improved cross-range resolution, thus, high resolution images can be obtained. Time-frequency transforms also allows the use of variable parameters that change according to the time and frequency, in order to achieve the desired target resolution [21].

In ISAR, due to complex motion of the target, the Doppler frequency content obtained by conventional Fourier transforms is time-varying. This leads the Doppler spectrum and image to be smeared. The time-varying Doppler frequency shift can be treated as time-invariant in each time slice by using the time-frequency transform; hence the image smearing effect will be suppressed and high resolution images can be obtained. The Doppler frequency resolution, which determines the cross-range resolution, is determined by the resolution of the selected time-frequency transform technique. There are various time-frequency transforms such as short-time Fourier transform (STFT) and wavelet transforms and bi-linear transforms such as Wigner-Ville and Choi-Williams. Many of these techniques will be examined throughout the thesis.

4.2 Time-Frequency Image Formation

Figure 4.2 and Figure 4.1 shows the basics of the target imaging using the time-frequency analysis. The difference from the conventional radar imaging system is that the Fourier transform is replaced by the time-frequency transform and time sampling. The Fourier-based system generates only one image frame from an $M \times N$ I and Q data where the radar transmits a sequence of N pulses and the total number of range cells is M . However, time-frequency based system generates $N \times N$ time-Doppler distribution for each time history series by taking the time-frequency transform of each one. Combining the M time-Doppler distributions at M range cells we end up with the $N \times M \times N$ time-range-Doppler cube $Q(r_m, f_n, t_n)$. It can be defined as:

$$Q(r_m, f_n, t_n) = TFT_n\{G(r_{m,n})\} \quad (4.4)$$

where $G(r_{m,n})$ is the range profiles with M time history series which are N pulses long and TFT_n denotes the Time-frequency operation which calculates the instantaneous Doppler frequency shift.

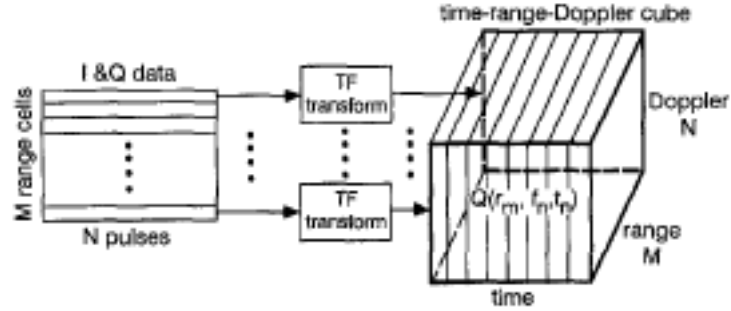


Figure 4.1: Obtaining the time-range-Doppler cube by time-frequency based image formation [11]

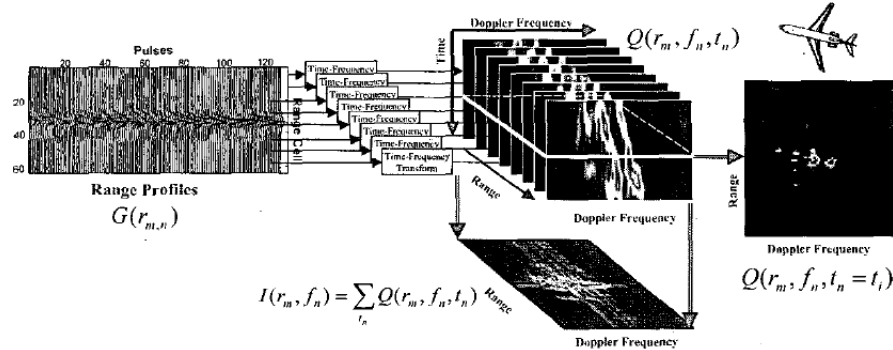


Figure 4.2: Time-sampling in time-frequency based image formation [9]

At a sampling time, t_i , only one range-Doppler image $Q(r_m, f_n)$ can be extracted from the cube $Q(r_m, f_n, t_n)$ which is the sum of N full range-Doppler images at particular time instants. Thus, by applying time-sampling we obtain a time sequence of 2D range-Doppler images. Each time sampled frame corresponds to a clear image of the target. The only advantage is not obtaining clear images with superior resolution, we can observe the time-varying properties of the target as well [21], [7].

To apply time-frequency techniques two different simulated data that are both provided by Victor C. Chen [3] are used. These are respectively:

- Simulated Mig-25 data: The stepped-frequency radar operates at 9GHz and has a bandwidth of 512MHz. For each pulse, 64 complex range samples were saved (64 pulses). 512 burst of pulses are used. The pulse repetition frequency is 15KHz. Basic motion compensation processing without polar reformation has been applied to the data without pulse compression. [3].
- Simulated Boeing-727 data: The stepped-frequency radar operates at 9GHz and has a bandwidth of 150 MHz. For each pulse, 64 complex range samples were saved. 256 burst of pulses are used. The pulse repetition frequency is 20KHz. Motion compensation and range processing have been applied to the data [3].

The images reconstructed by conventional Fast Fourier Transform (FFT) technique are shown in Figure 4.3. These images can be compared with the images reconstructed by various time-frequency transforms that will be introduced in the following sections. The discussions about the obtained images will be made in Section 5.5 together with the other simulation results in Chapter 5.

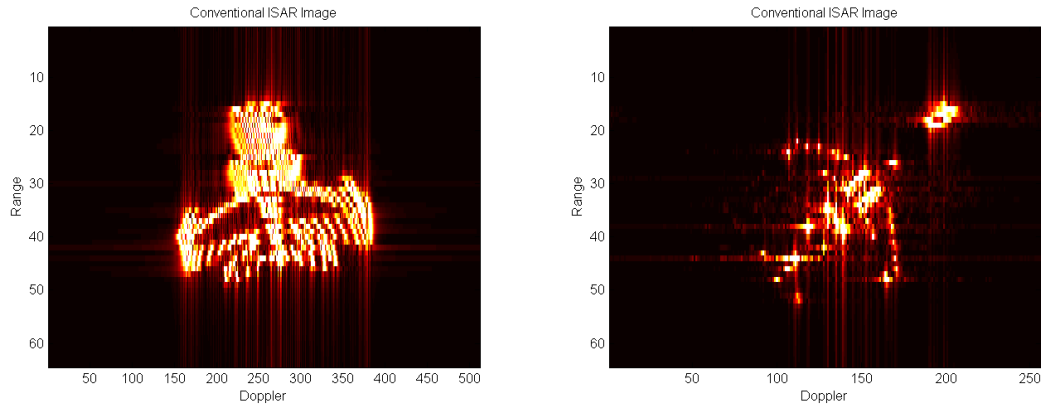


Figure 4.3: Original ISAR image created by regular FFT approach

4.3 Linear Time-Frequency Transforms

Linearity is one of the most desirable property in any application involving multicomponent signals such as speech and radar signals:

$$s(t) = c_1 s_1(t) + c_2 s_2(t) \Rightarrow T_x(t, f) = c_1 T_{x_1}(t, f) + c_2 T_{x_2}(t, f) \quad (4.5)$$

where $s_1(t)$ and $s_2(t)$ are two different signals and $T_{x_1}(t, f)$ and $T_{x_2}(t, f)$ represent the time-frequency transform of the signals.

Some of the linear time-frequency transforms are short-time Fourier transform (STFT), continuous wavelet transform (CWT) and the adaptive time-frequency transforms. Since it is the most known, only STFT will be discussed in this chapter.

4.3.1 Short-Time Fourier Transform

Short-time Fourier transform is one of the most known time-frequency transforms. A moving window Fourier transform is the basic idea behind STFT [21]. Time localization of frequency components of the a signal can be obtained by suitably pre-windowing the signal $s(t)$:

$$STFT(t, w) = \int s(t') w(t - t') e^{-j\omega t'} dt' \quad (4.6)$$

The function $w(t)$ is named the *window function* since usually it has a short time duration. By moving $w(t)$ and repeating the same process in Equation (4.6), we can roughly observe the signal's frequency contents change over time.

STFT indicates a signal's behaviour in the vicinity of $[t - \Delta_t, t + \Delta_t]x[w - \Delta_w, w + \Delta_w]$. Δ_t and Δ_w are desired to be as narrow as possible in order to better measure a signal at a particular time and frequency. Unfortunately the selections of Δ_t and Δ_w are related via Fourier transform (see Equation 4.1) and limited by the uncertainty principle (see Equation 4.3). Thus STFT has limited time-frequency resolution which is determined by the size of the window used. The uncertainty principle prohibits using arbitrarily small duration and arbitrarily small bandwidth windows. A fundamental resolution trade-off exists: a smaller window has a higher time resolution but a lower frequency resolution whereas a larger window has higher frequency resolution but a lower time resolution [32].

Images of simulated MIG-25 and Boeing-727 reconstructed by STFT using M/4 and M/32 length hamming windows are shown in Figure 4.4, Figure 4.5, Figure 4.6 and Figure 4.7,

respectively (M is the total number of bursts of pulses which is 512 for MIG-25 and 256 for Boeing 727 data):

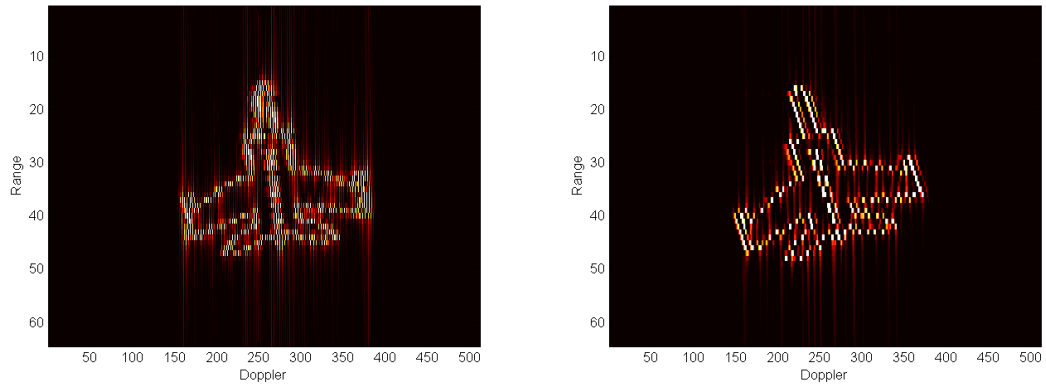


Figure 4.4: Images of simulated MIG-25 reconstructed by STFT using $M/4$ length windows.

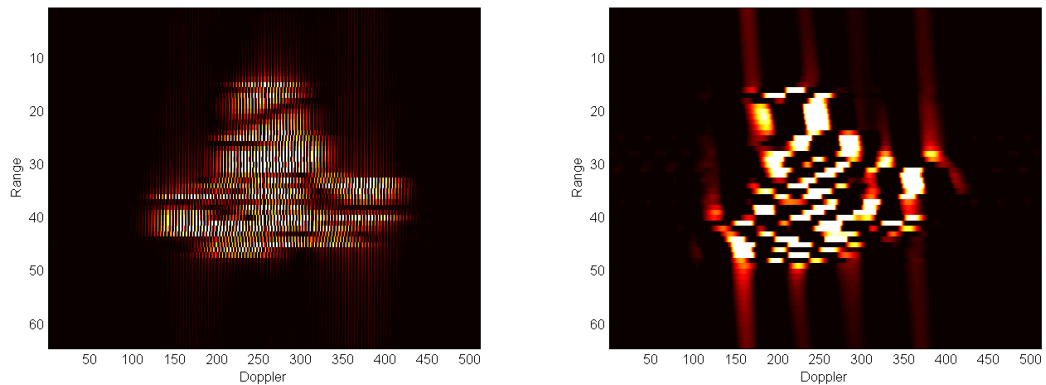


Figure 4.5: Images of simulated MIG-25 reconstructed by STFT using $M/32$ length windows.

4.4 Bi-linear Time-Frequency Transforms

Power spectrum of a signal $s(t)$, which is the magnitude square of its Fourier transform, $|S(W)|$, characterizes the signal's energy distribution in the frequency domain:

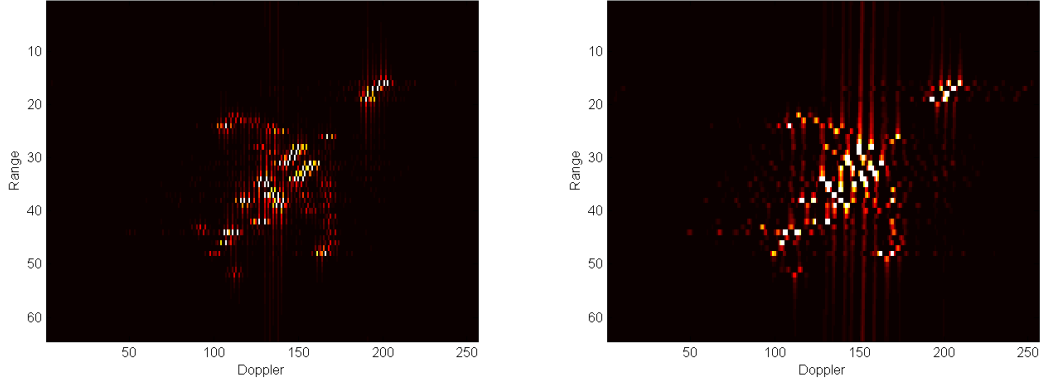


Figure 4.6: Images of simulated Boeing-727 reconstructed by STFT using $M/4$ length windows.

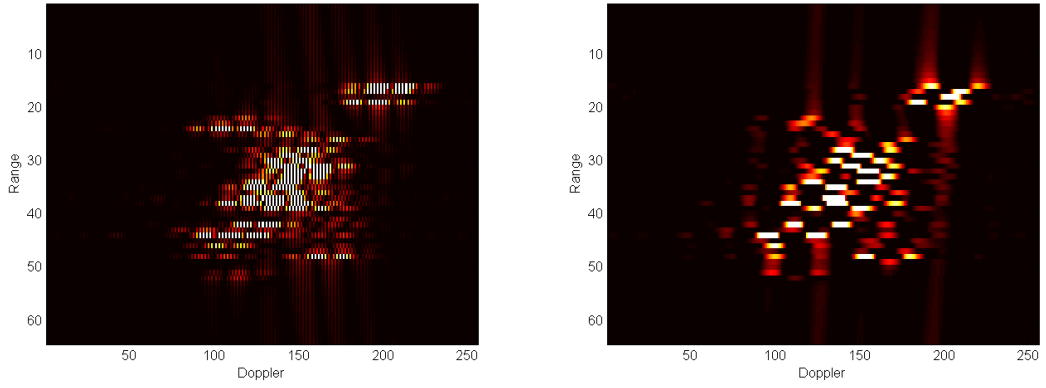


Figure 4.7: Images of simulated Boeing-727 reconstructed by STFT using $M/32$ length windows.

$$P(t, w) = |S(W)|^2 = \int_{-\infty}^{\infty} R(\tau) e^{-jw\tau} d\tau \quad (4.7)$$

where the auto-correlation function is given by:

$$R(\tau) = s(t) s^*(t - \tau) dt \quad (4.8)$$

Based on Equation (4.7) it is not possible to tell whether or not the signal's power

spectrum changes over time. Thus, the standard power spectrum is insufficient to represent signals whose frequency content change over time. To depict a time-dependent spectrum and to achieve high resolution in both time and frequency domains, a time dependent auto-correlation function $R(t, \tau)$ can be used. The Fourier transform of a time dependent auto-correlation function $R(t, \tau)$ gives us the time-dependent power spectrum of the signal $s(t)$:

$$P(t, w) = \int_{-\infty}^{\infty} R(t, \tau) e^{-jw\tau} d\tau \quad (4.9)$$

The power spectrum is the quadratic function of frequencies. The linearity of the STFT can not be applied to the quadratic signals. The power spectrum of the sum of two signals $s_1(t) + s_2(t)$ is not simply the sum of the individual power spectrum $P_1(t, w) + P_2(t, w)$. The quadratic superposition principle is given for any time frequency distribution (TFD) as:

$$\begin{aligned} s(t) &= c_1 s_1(t) + c_2 s_2(t) \Rightarrow \\ T_s(t, f) &= |c_1|^2 T_{s_1}(t, f) + |c_2|^2 T_{s_2}(t, f) + c_1 c_2^* T_{s_1 s_2}(t, f) + c_2 c_1^* T_{s_2 s_1}(t, f) \end{aligned} \quad (4.10)$$

where $T_{x_1 x_2}(t, f)$ and $T_{x_2 x_1}(t, f)$ are the cross-terms of the signals $s_1(t)$ and $s_2(t)$.

We can generalize the quadratic superposition principle to an N-component signal:

$$s(t) = \sum_{i=1}^N c_i s_i(t) \quad (4.11)$$

such that there corresponds an auto-term $|c_i|^2 T_{s_i}(t, f)$ for each signal component $c_i s_i(t)$ and there corresponds a cross-term (interference term) $c_i c_j^* T_{s_i s_j}(t, f) + c_j c_i^* T_{s_j s_i}(t, f)$ for each pair of signal components $c_i s_i(t)$ and $c_j s_j(t)$.

It should be noted that the number of cross-terms grows quadratically as the number of signal components increase since for an N-component signal there exists N auto-terms and $N(N - 1)/2$ cross-terms [19].

Throughout this chapter many quadratic (bi-linear) distributions will be discussed, starting with the most known, which is Wigner-Ville distribution:

4.4.1 Wigner-Ville Distribution

The first developed so that the most significant of the bi-linear time-frequency transforms is the Wigner-Ville Distribution (WVD). It is originally developed in the area of quantum mechanics by Wigner in 1932 and introduced for signal analysis by a French scientist Ville in 1947 [21].

In the WVD, the time-dependent auto-correlation function is chosen to be:

$$R(t, \tau) = s\left(t + \frac{\tau}{2}\right) s^*\left(t - \frac{\tau}{2}\right) \quad (4.12)$$

Substituting Equation (4.12) into Equation (4.9), we obtain the WVD as:

$$WVD(t, w) = \int s\left(t + \frac{\tau}{2}\right) s^*\left(t - \frac{\tau}{2}\right) e^{-jw\tau} d\tau \quad (4.13)$$

Unlike the STFT there is no time-limited window in WVD. It provides both higher time and frequency resolution compared to STFT. However, when the signal contains more than one component, the WVD generates cross-term interference terms between each pair of signal components. The cross-terms generated are highly oscillatory and have limited energy. Although these terms have limited contribution to signal energy, they usually degrade the time-frequency spectrum's useful range [9].

ISAR images of simulated MIG-25 and simulated Boeing-727 reconstructed using Wigner-Ville distribution are shown in Figure 4.8 and Figure 4.9, respectively:

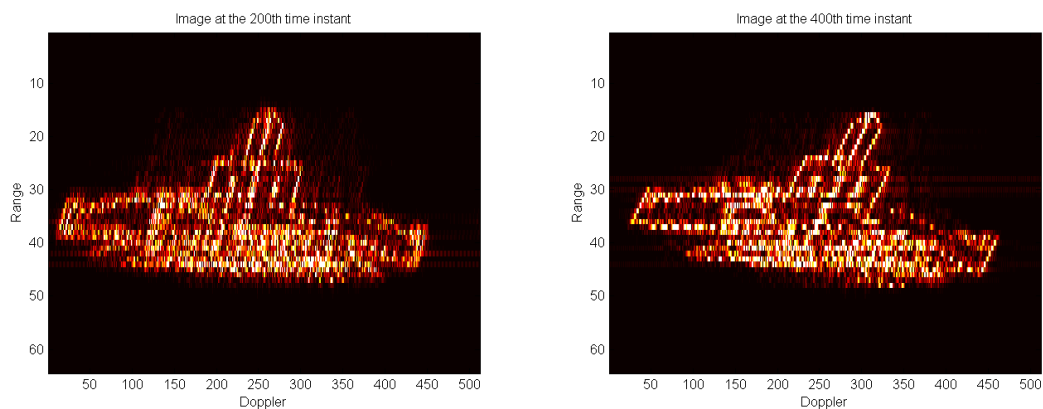


Figure 4.8: Images of simulated MIG-25 reconstructed using Wigner-Ville distribution

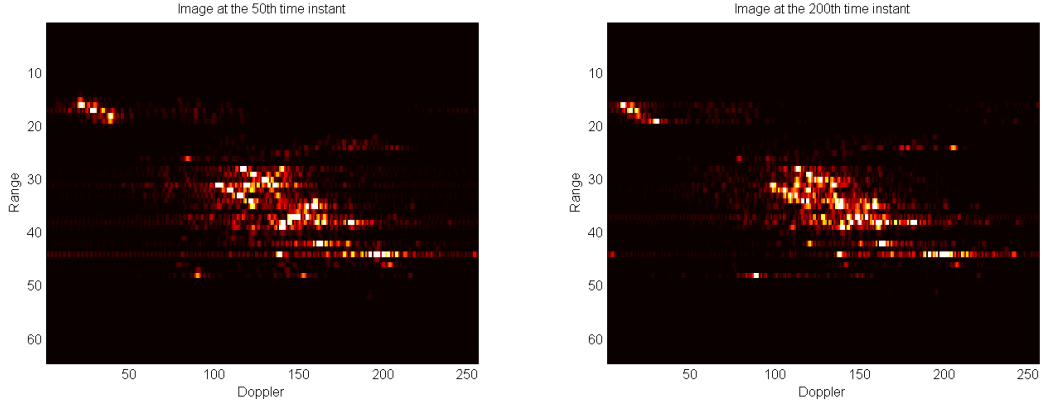


Figure 4.9: Images of simulated Boeing-727 reconstructed using Wigner-Ville distribution

To reduce the cross-term interference, the 2D filtered (a unique kernel function) WVD can be used. Thus, cross-term interference can be reduced significantly while time-frequency resolution is slightly reduced.

Leon Cohen showed that all existing time-frequency distributions could be written in a generalized form [14] and new time-frequency transforms can be derived using this form [15]. This class of transforms are known as Cohen's class. The generalized form is defined as:

$$C(t, w) = \int \int s(u + \frac{\tau}{2}) s^*(u - \frac{\tau}{2}) \phi(t - u, \tau) e^{-jw\tau} du d\tau \quad (4.14)$$

where the Fourier transform of $\phi(t, \tau)$ gives us the kernel function $\Phi(\theta, \tau)$. If we choose the kernel function as $\Phi(\theta, \tau) = 1$, then $\phi(t, \tau) = \delta(t)$ thus giving us the WVD. As seen WVD is a member of Cohen's class.

There are many other time-frequency distributions in Cohen's class each with a unique, signal independent kernel function. Pseudo Wigner-Wille (PWV), smoothed pseudo Wigner-Ville (SPWV), Choi-Williams (CW), Zhao-Atlas-Marks (ZAM), Born-Jordan, Butterworth, Cone-kernel, Generalized exponential, Levin, Page, Rihaczek are some of the distributions that are considered to be members of Cohen's class [19].

4.4.2 Pseudo Wigner-Ville Distribution

The PWVD is one of Cohen's class distribution as the other distributions that will be discussed further. PWVD has reduced cross-term interference. It has the advantage over the spectrogram of instantaneous temporal response, but it still produces some interfering

cross-terms when used in multicomponent signal analysis. PWVD is mathematically defined as:

$$PWVD(t, u) = \int h(\tau) s(t + \frac{\tau}{2}) s^*(t - \frac{\tau}{2}) e^{-j2\pi u\tau} d\tau \quad (4.15)$$

where h is the frequency smoothing window.

ISAR images of simulated MIG-25 and simulated Boeing-727 reconstructed using pseudo Wigner-Ville distribution are shown in Figure 4.10 and Figure 4.11, respectively:

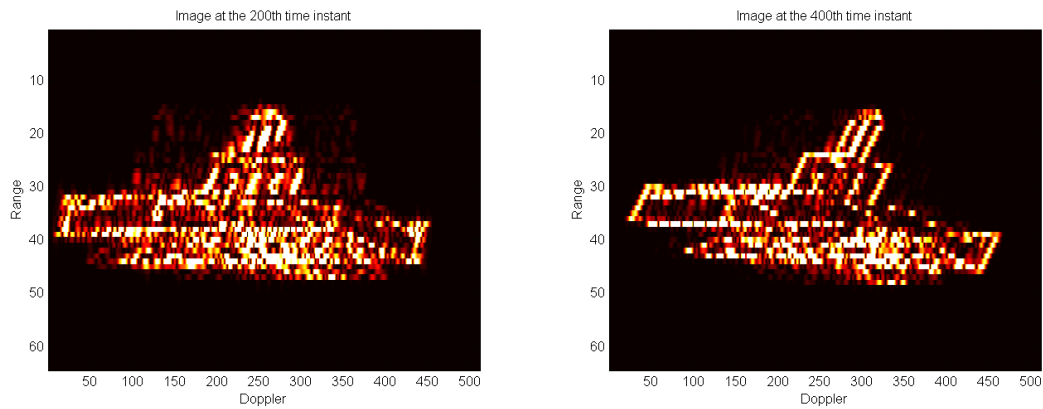


Figure 4.10: Images of simulated MIG-25 reconstructed using pseudo Wigner-Ville distribution

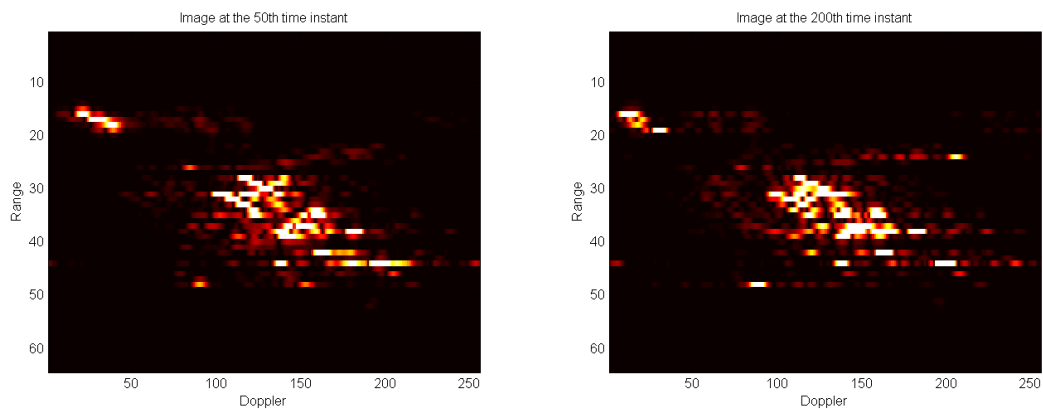


Figure 4.11: Images of simulated Boeing-727 reconstructed using pseudo Wigner-Ville distribution

4.4.3 Smoothed Pseudo Wigner-Ville Distribution

The SPWVD has a Gaussian smoothed window, it suppresses cross-terms in WVD, but the resolution is also reduced. Most of the images from the SPWVD have higher resolution than those produced by the STFT using the same data. Smoothing the WVD, cross-term interference can highly be reduced but some phase information is lost. The distribution can be written in the following form [32]:

$$SPWVD(t, v, ; g, h) = \int h(\tau) \int g(s - t) x(s + \frac{\tau}{2}) x^*(s - \frac{\tau}{2}) e^{-j2\pi v\tau} d\tau \quad (4.16)$$

where h is the frequency smoothing window where as g is the time smoothing window.

ISAR images of simulated MIG-25 and simulated Boeing-727 reconstructed using smoothed pseudo Wigner-Ville distribution are shown in Figure 4.12 and Figure 4.13, respectively:

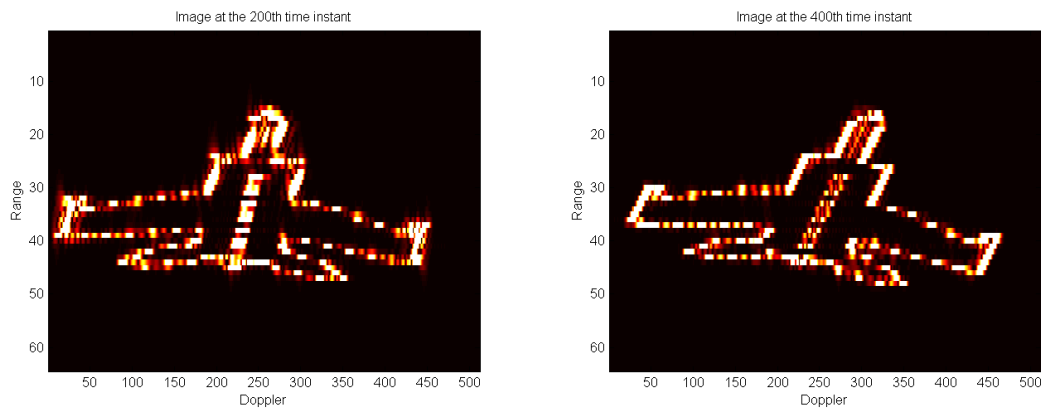


Figure 4.12: Images of simulated MIG-25 reconstructed using smoothed pseudo Wigner-Ville distribution

4.4.4 Choi-Williams Distribution

The Choi-Williams distribution is a smoothed version of WVD with a defined kernel [13]. It is a shift-invariant transform. The kernel function is defined as:

$$\Phi(\theta, \tau) = e^{-\alpha(\theta\tau)^2} \quad (4.17)$$

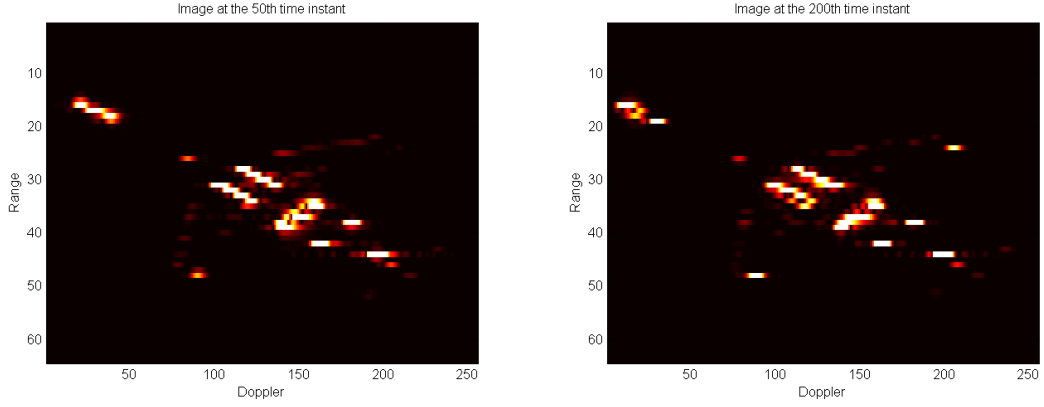


Figure 4.13: Images of simulated Boeing-727 reconstructed using smoothed pseudo Wigner-Ville distribution

The inverse Fourier transform of this exponential kernel is:

$$\phi(t, \tau) = \frac{1}{\sqrt{4\pi\alpha\tau^2}} e^{-\frac{1}{4\alpha\tau^2}t^2} \quad (4.18)$$

Thus using Equation (4.14) and Equation (4.18):

$$CWD_x(t, v) = \int \int \frac{1}{\sqrt{4\pi\alpha\tau^2}} e^{-\frac{(t-u)^2}{4\alpha\tau^2}} s(u + \frac{\tau}{2}) s^*(u - \frac{\tau}{2}) e^{-jv\tau} du d\tau \quad (4.19)$$

The corresponding kernel function is a low-pass filter in the $\xi - \tau$ plane. The smoothing is controlled by the constant σ . The larger the σ is, the more the more cross-terms are suppressed but it also means the more the auto-terms are affected. Therefore, a trade-off for the selection of the parameter σ exists. It can be also noted that, the CWD will simply converge to WVD as $\sigma \rightarrow \infty$ and kernel goes to 1.

The exponential kernel preserves all cross-terms that are in the $\theta - \tau$ plane while it suppresses the portion that is away from the origin. As a result, the CWD usually contains strong horizontal and vertical ripples. This ripples are caused by the auto-terms that have the same frequency center and the same time center [2], [28].

ISAR images of simulated MIG-25 and simulated Boeing-727 reconstructed using Choi-Williams distribution are shown in Figure 4.14 and Figure 4.15, respectively:

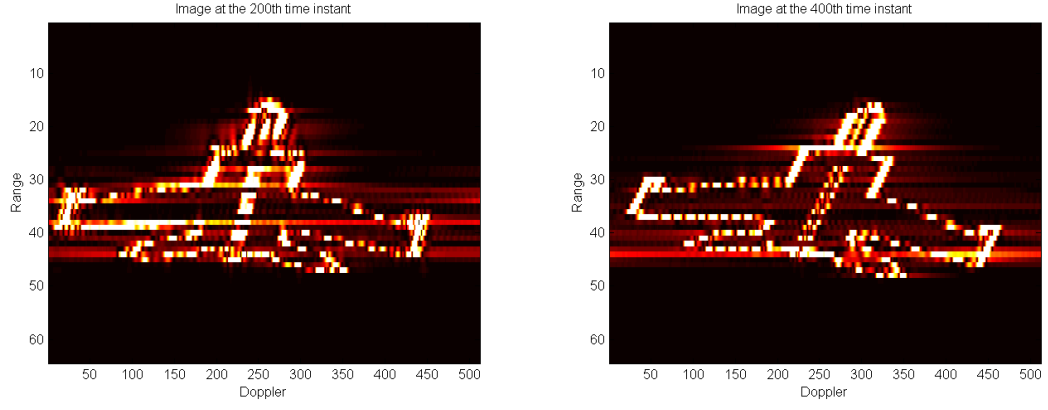


Figure 4.14: Images of simulated MIG-25 reconstructed using Choi-Williams distribution

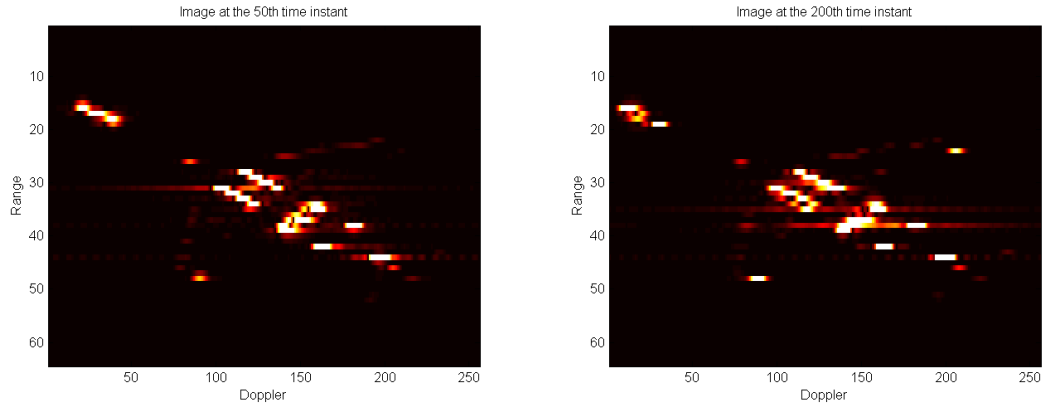


Figure 4.15: Images of simulated Boeing-727 reconstructed using Choi-Williams distribution

4.4.5 Born-Jordan Distribution

Born-Jordan distribution is a shift invariant, kernel smoothed version of WVD. The distribution performs well for signals with constant frequency whereas it does not perform as well for signal with frequency modulation [32]. The kernel function is defined as:

$$\Phi(\theta, \tau) = \frac{\sin(\pi\theta\tau)}{\pi\theta\tau} \quad (4.20)$$

Thus, the BJD is:

$$BJ_x(t, v) = \int_{-\infty}^{\infty} \frac{1}{|\tau|} \int_{t+|\tau|/2}^{t+|\tau|/2} x\left(s + \frac{\tau}{2}\right) x^*\left(s - \frac{\tau}{2}\right) ds e^{-j2\pi v\tau} ds d\tau \quad (4.21)$$

ISAR images of simulated MIG-25 and simulated Boeing-727 reconstructed using Born-Jordan distribution are shown in Figure 4.16 and Figure 4.17, respectively:

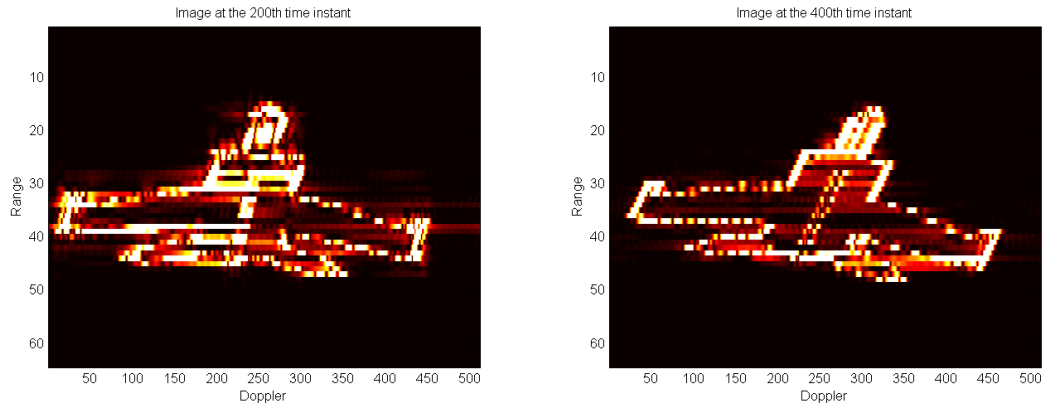


Figure 4.16: Images of simulated MIG-25 reconstructed using Born-Jordan distribution

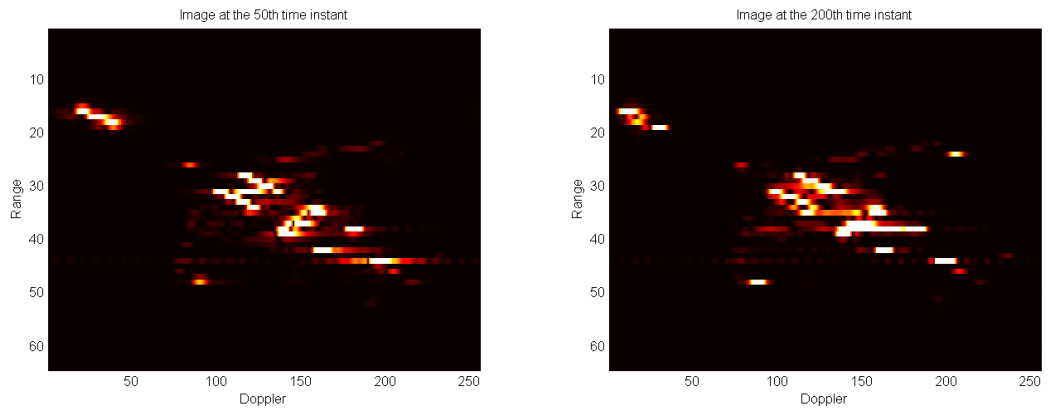


Figure 4.17: Images of simulated Boeing-727 reconstructed using Born-Jordan distribution

4.4.6 Zhao-Atlas-Marks Distribution

The Zhao-Atlas-Marks distribution is a widely used distribution. It is also called cone-shaped distribution (CSD) because of the definition of a cone-shaped $\phi(t, \tau)$:

$$\phi(t, \tau) = \begin{cases} g(\tau) & |\tau| \geq 2|t| \\ 0 & \text{otherwise} \end{cases} \quad (4.22)$$

If

$$g(\tau) = \frac{1}{\tau} e^{-\alpha\tau^2} \quad (4.23)$$

Then the kernel function becomes:

$$\Phi(\theta, \tau) = \frac{\sin(\theta\tau/2)}{\theta\tau/2} e^{-\alpha\tau^2} \quad (4.24)$$

Thus using Equation (4.14), the distribution becomes [37]:

$$ZAM_x(t, v) = \int_{-\infty}^{\infty} \left\{ g(\tau) \int_{t+|\tau|/2}^{t+|\tau|/2} x\left(s + \frac{\tau}{2}\right) x^*\left(s - \frac{\tau}{2}\right) ds \right\} e^{-j2\pi v\tau} d\tau \quad (4.25)$$

The suppression degree is controlled by the parameter α . A large α suppresses the cross-terms more at the expense of more disturbed auto-terms [28].

Unlike the exponential kernel function used in CWD (4.18), the cone-shaped kernel can suppress the cross-terms created by the auto-terms that have the same frequency center. Therefore cross-term interference is significantly reduced in CSD compared to CWD [28].

ISAR images of simulated MIG-25 and simulated Boeing-727 reconstructed using Zhao-Atlas-Marks distribution are shown in Figure 4.18 and Figure 4.19, respectively:

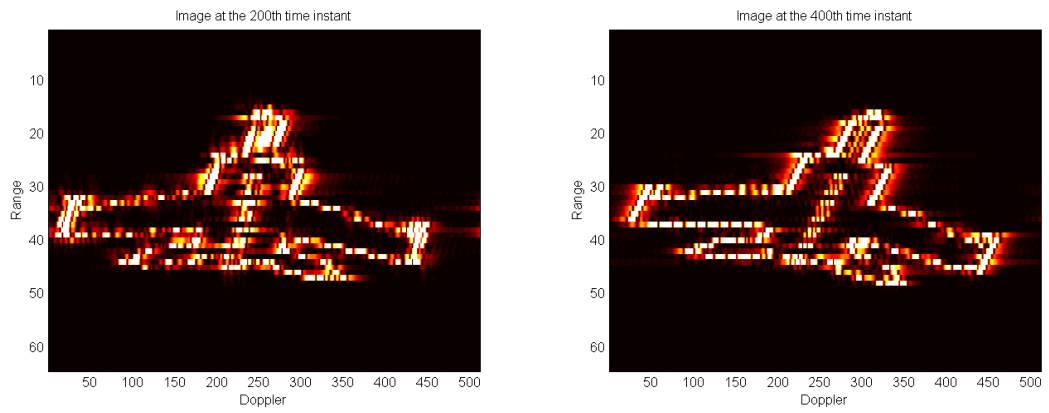


Figure 4.18: Images of simulated MIG-25 reconstructed using Zhao-Atlas-Marks distribution

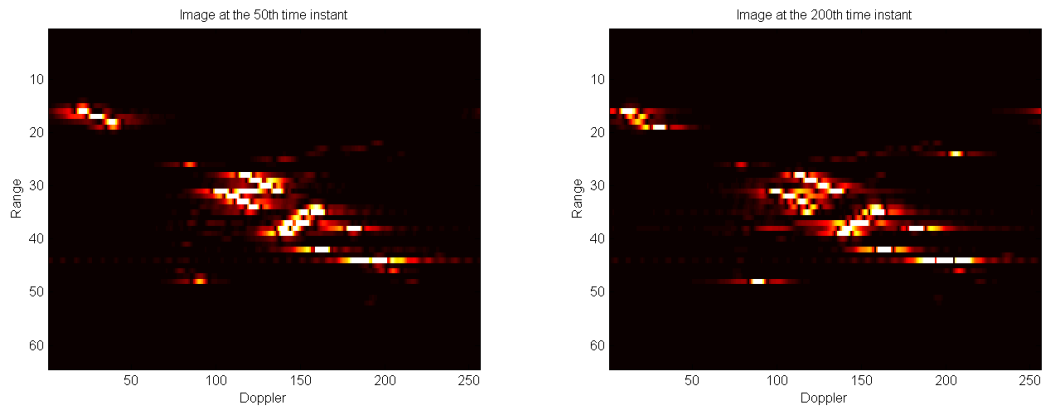


Figure 4.19: Images of simulated Boeing-727 reconstructed using Zhao-Atlas-Marks distribution

CHAPTER 5

PERFORMANCE ANALYSIS OF TIME-FREQUENCY TRANSFORMS FOR VARIOUS COMPLEX MANOEUVRING TARGET SCENARIOS

5.1 Introduction

In this chapter, all the time-frequency transforms introduced in Chapter 4 are applied and compared for three different scenarios. The stepped-frequency ISAR simulation is described in sections 3.3 and 3.5. The target model is defined in 3.4 and the scenarios are defined in 3.6. Since the same scenarios are used, the performance comparison of time-frequency transforms with conventional Fourier transform can also be done. The discussion on performances of the transforms is done in section 5.5 after all the results are shown.

5.2 Scenario 1: Target with Yaw Motion

Conventional Fourier Transform

The image reconstructed by conventional method that uses Fourier transform is shown in Figure 3.3

Short-Time Fourier Transform

The images reconstructed by STFT using $M/4$ and $M/32$ length Hamming windows are shown in Figure 5.1 and Figure 5.2 respectively. Note that M is the total number of bursts of pulses which is 512 in our simulation.

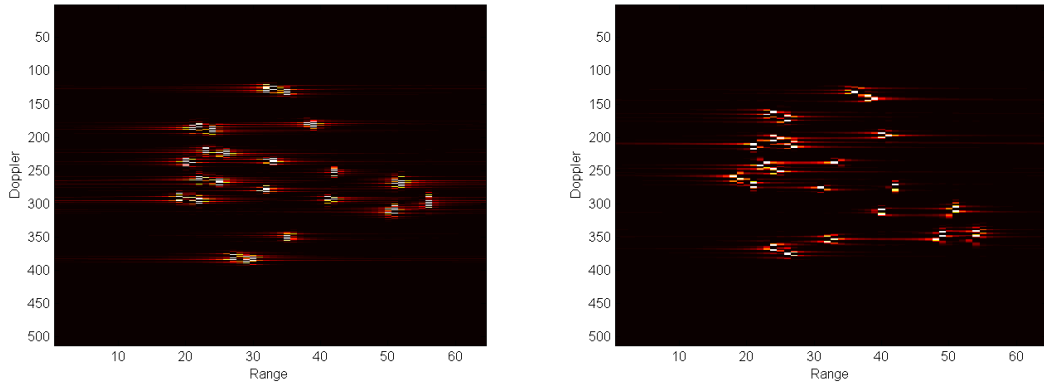


Figure 5.1: Scenario 1: Images reconstructed by STFT using $M/4$ length windows.

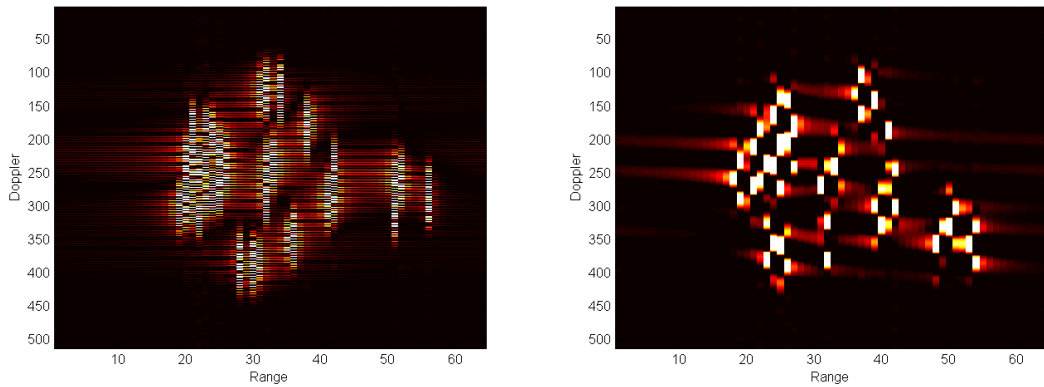


Figure 5.2: Scenario 1: Images reconstructed by STFT using $M/32$ length windows.

Wigner-Ville Distribution

Images reconstructed using Wigner-Ville distribution are shown in Figure 5.3.

Pseudo Wigner-Ville Distribution

Images reconstructed using pseudo Wigner-Ville distribution are shown in Figure 5.4.

Smoothed Pseudo Wigner-Ville Distribution

Images reconstructed using smoothed pseudo Wigner-Ville distribution are shown in Figure 5.5.

Choi-Williams Distribution

Images reconstructed using Choi-Williams distribution are shown in Figure 5.6.

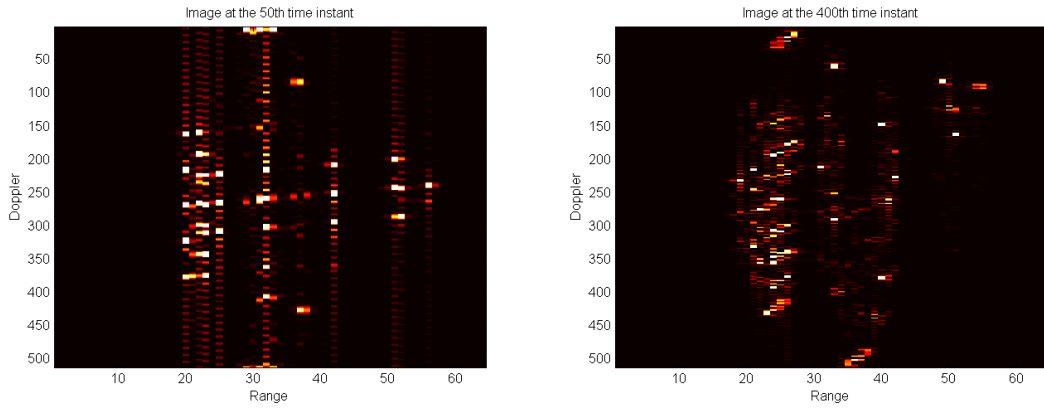


Figure 5.3: Scenario 1: Images reconstructed using Wigner-Ville distribution

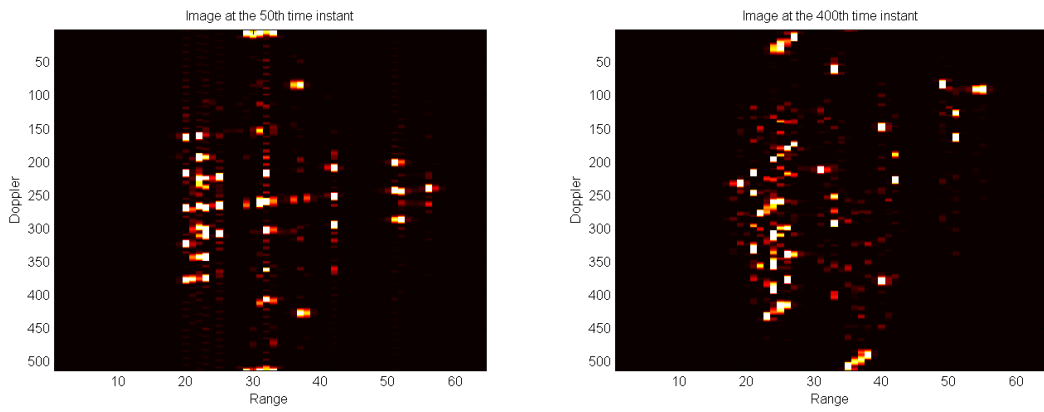


Figure 5.4: Scenario 1: Images reconstructed using pseudo Wigner-Ville distribution

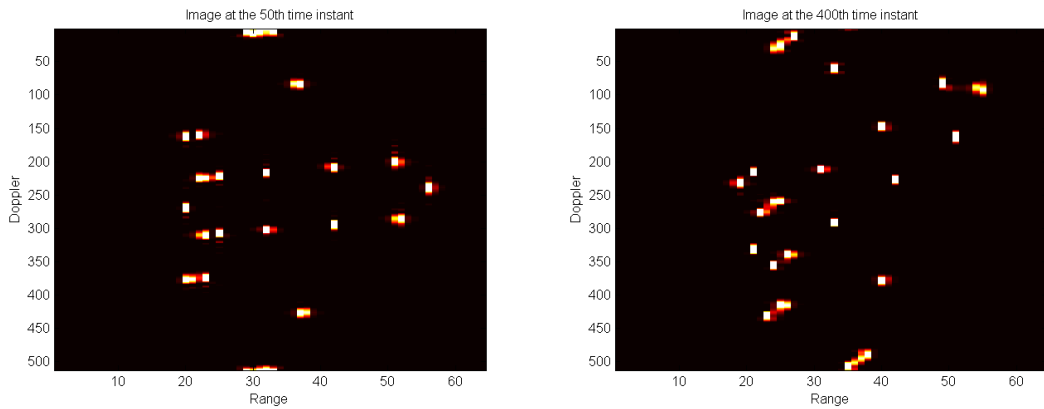


Figure 5.5: Scenario 1: Images reconstructed using smoothed pseudo Wigner-Ville distribution

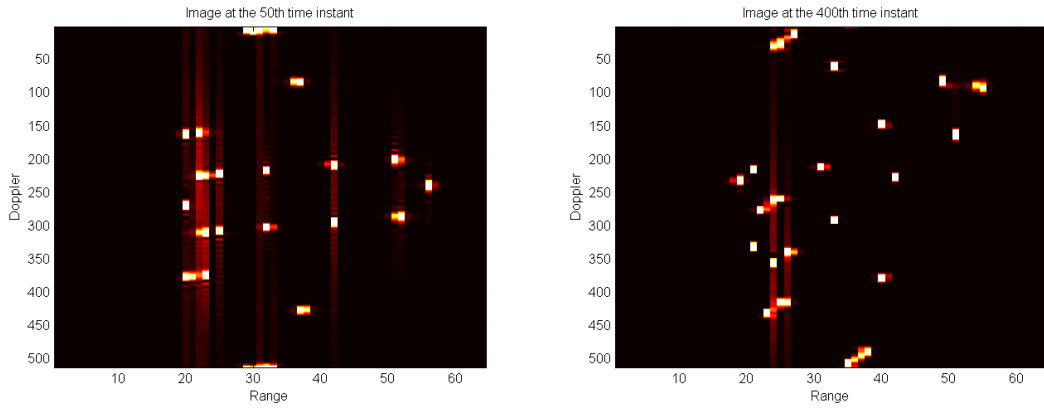


Figure 5.6: Scenario 1: Images reconstructed using Choi-Williams distribution

Born-Jordan Distribution

Images reconstructed using Born-Jordan distribution are shown in Figure 5.7.

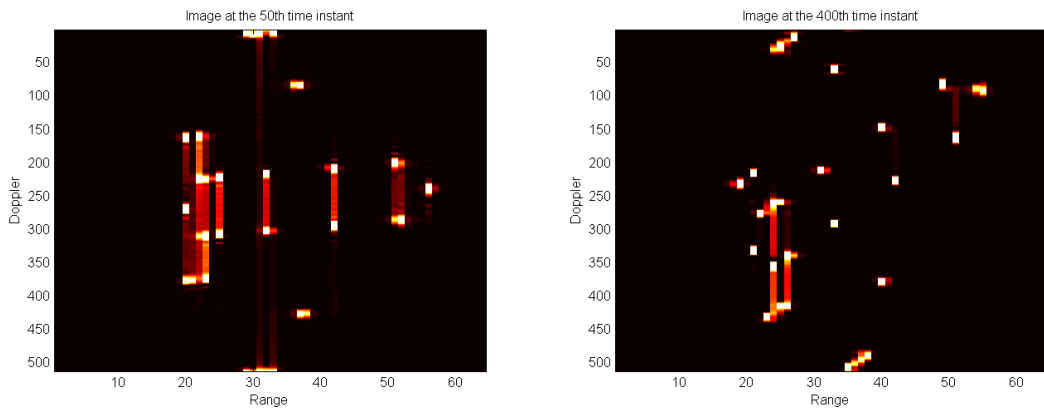


Figure 5.7: Scenario 1: Images reconstructed using Born-Jordan distribution

Zhao-Atlas-Marks Distribution

Images reconstructed using Zhao-Atlas-Marks distribution are shown in Figure 5.8.

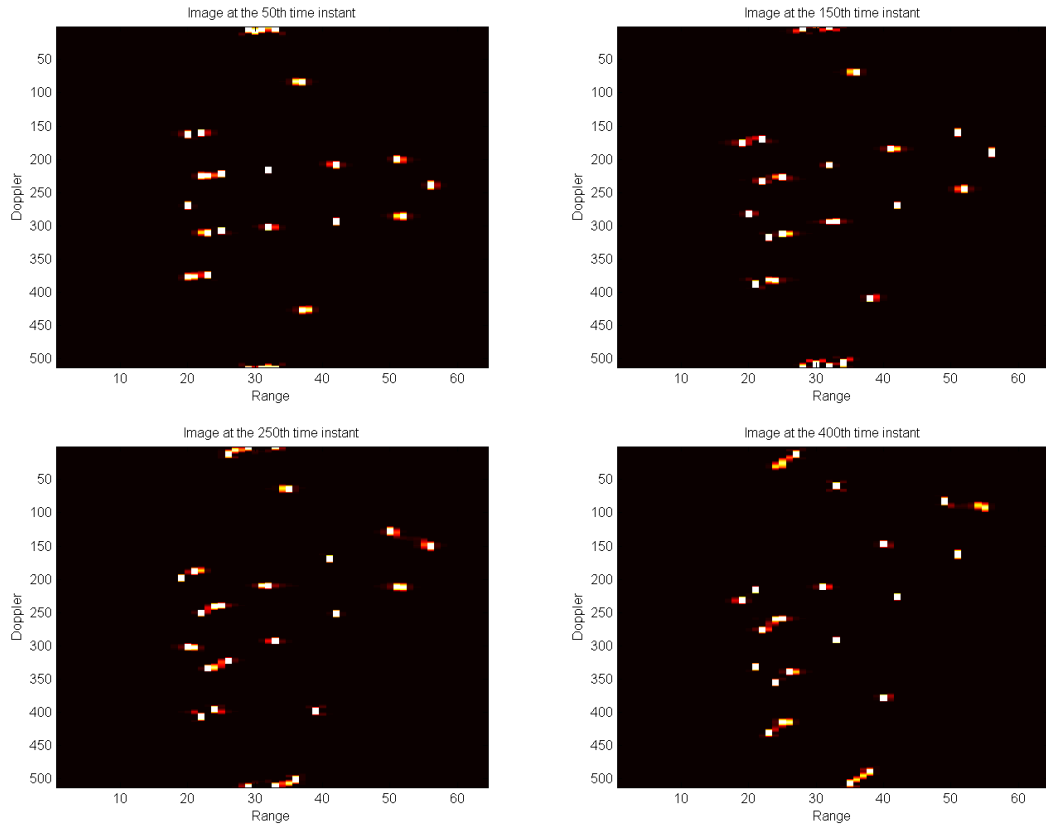


Figure 5.8: Scenario 1: Images reconstructed using Zhao-Atlas-Marks distribution

5.3 Scenario 2: Target with Yaw and Roll Motions

Conventional Fourier Transform

The image reconstructed by conventional method that uses Fourier transform is shown in Figure 3.4

Short-Time Fourier Transform

The images reconstructed by STFT using $M/4$ and $M/32$ length Hamming windows are shown in Figure 5.9, Figure 5.10 respectively. Note that M is the total number of bursts of pulses which is 512 in our simulation.

Wigner-Ville Distribution

Images reconstructed using Wigner-Ville distribution are shown in Figure 5.11.

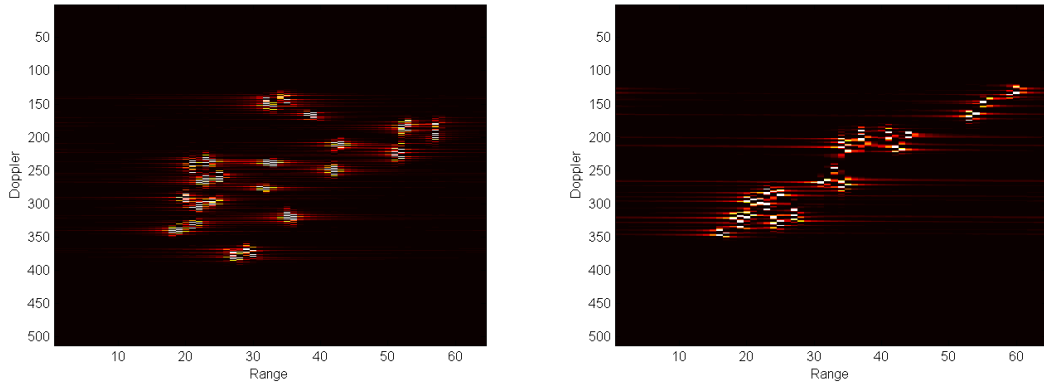


Figure 5.9: Scenario 2: Images reconstructed by STFT using $M/4$ length windows.

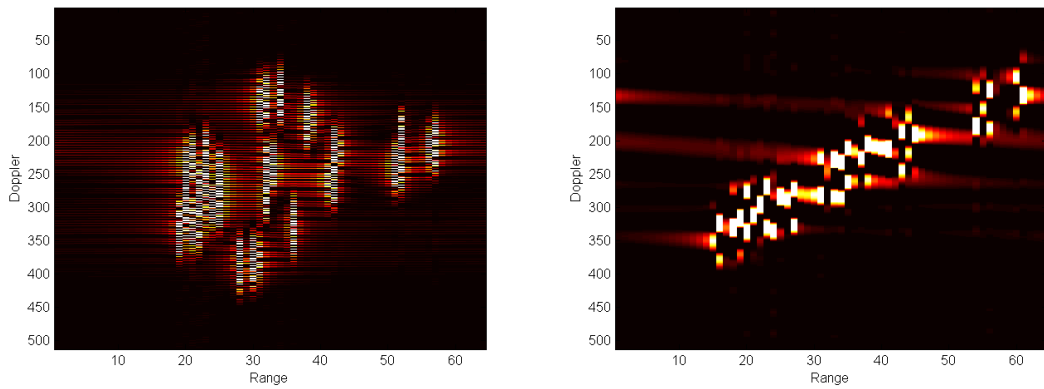


Figure 5.10: Scenario 2: Images reconstructed by STFT using $M/32$ length windows.

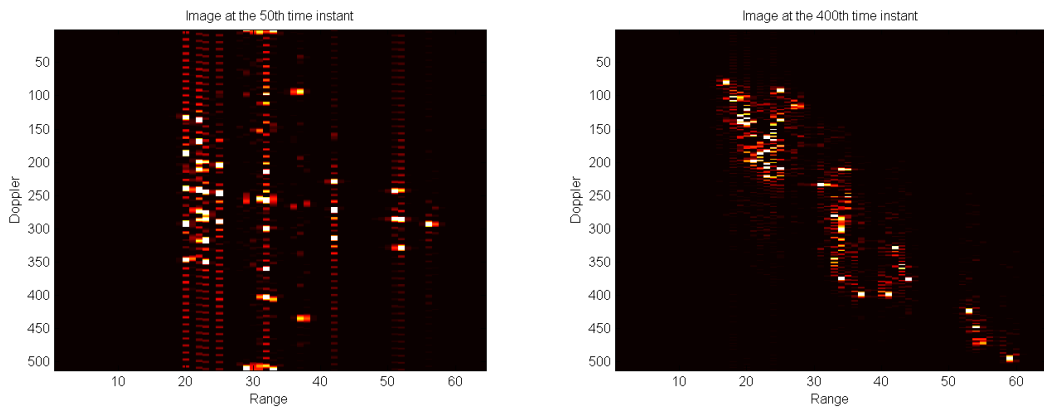


Figure 5.11: Scenario 2: Images reconstructed using Wigner-Ville distribution

Pseudo Wigner-Ville Distribution

Images reconstructed using pseudo Wigner-Ville distribution are shown in Figure 5.12.

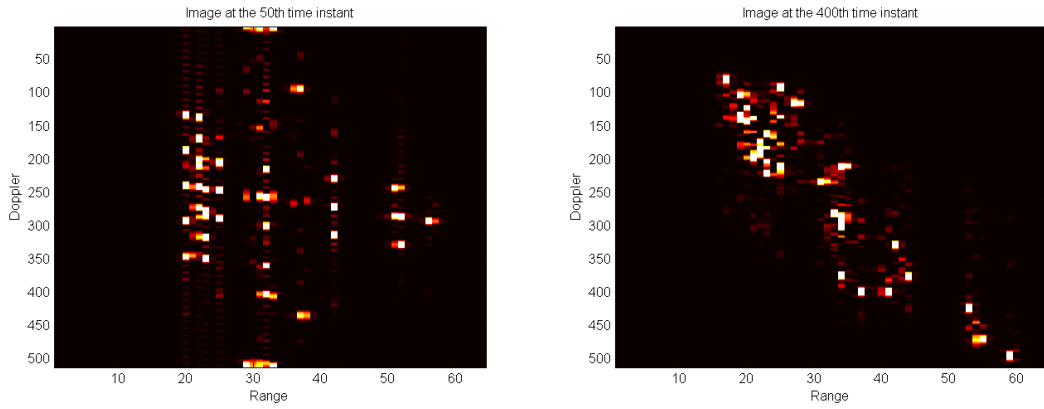


Figure 5.12: Scenario 2: Images reconstructed using pseudo Wigner-Ville distribution

Smoothed Pseudo Wigner-Ville Distribution

Images reconstructed using smoothed pseudo Wigner-Ville distribution are shown in Figure 5.13.

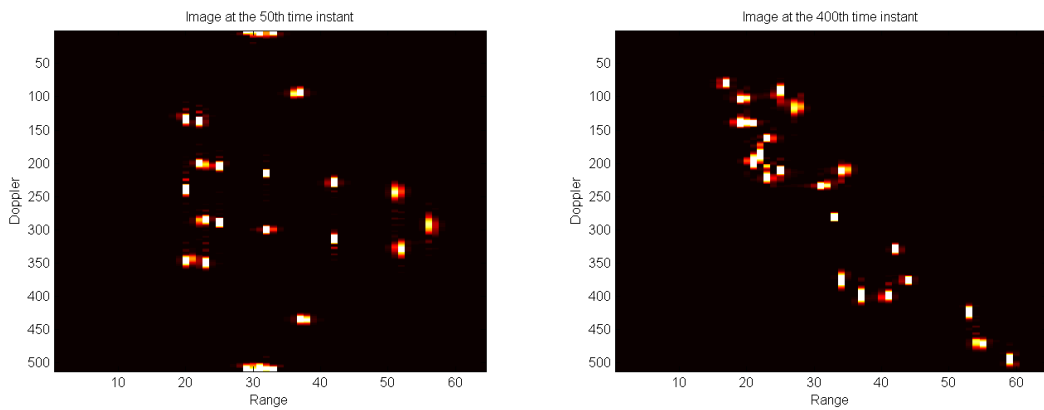


Figure 5.13: Scenario 2: Images reconstructed using smoothed pseudo Wigner-Ville distribution

Choi-Williams Distribution

Images reconstructed using Choi-Williams distribution are shown in Figure 5.14.

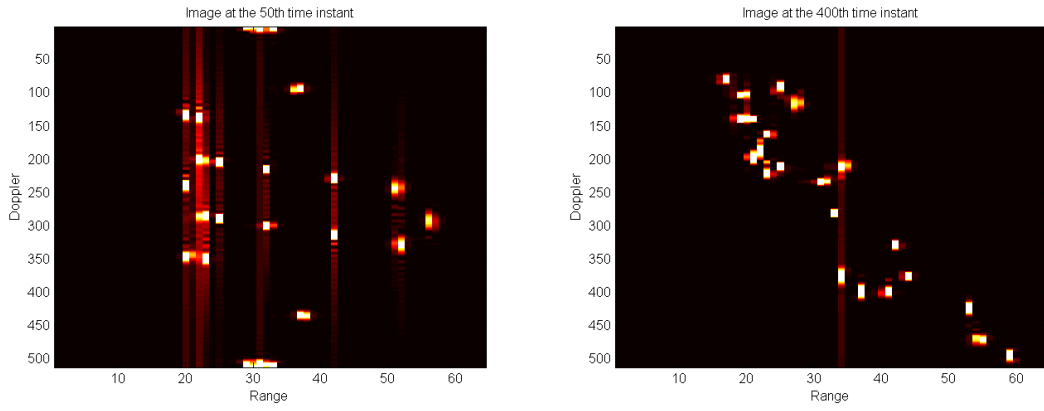


Figure 5.14: Scenario 2: Images reconstructed using Choi-Williams distribution

Born-Jordan Distribution

Images reconstructed using Born-Jordan distribution are shown in Figure 5.15.

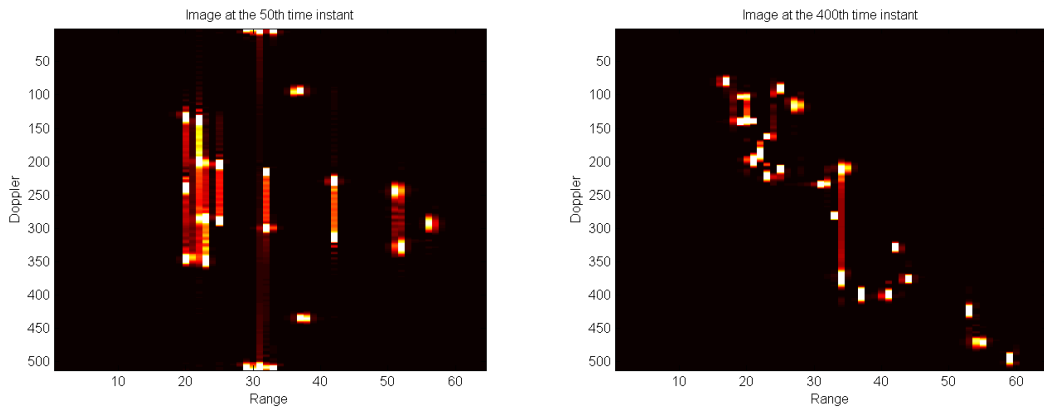


Figure 5.15: Scenario 2: Images reconstructed using Born-Jordan distribution

Zhao-Atlas-Marks Distribution

Images reconstructed using Zhao-Atlas-Marks distribution are shown in Figure 5.16.

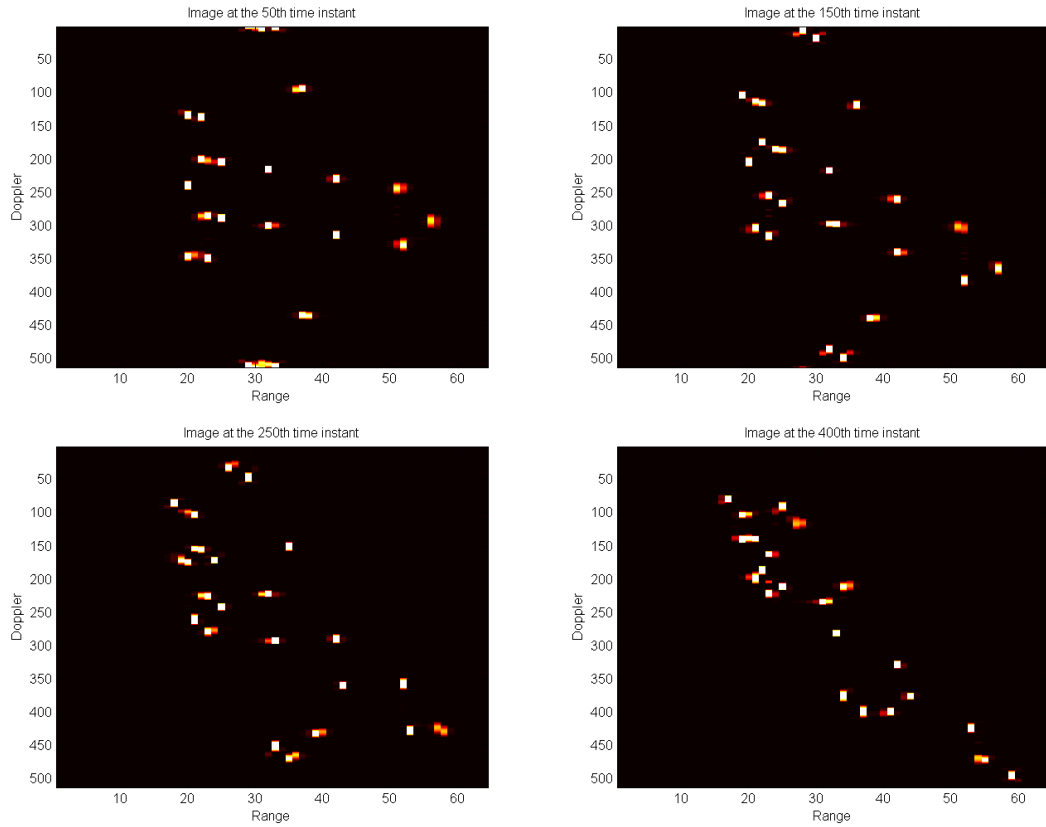


Figure 5.16: Scenario 2: Images reconstructed using Zhao-Atlas-Marks distribution

5.4 Scenario 3: Target with Yaw, Pitch and Roll Motions

Conventional Fourier Transform

The image reconstructed by conventional method that uses Fourier transform is shown in Figure 3.5

Short-Time Fourier Transform

The images reconstructed by STFT using $M/4$ and $M/32$ length Hamming windows are shown in Figure 5.17, Figure 5.18 respectively. Note that M is the total number of bursts of pulses which is 512 in our simulation.

Wigner-Ville Distribution

Images reconstructed using Wigner-Ville distribution are shown in Figure 5.19.

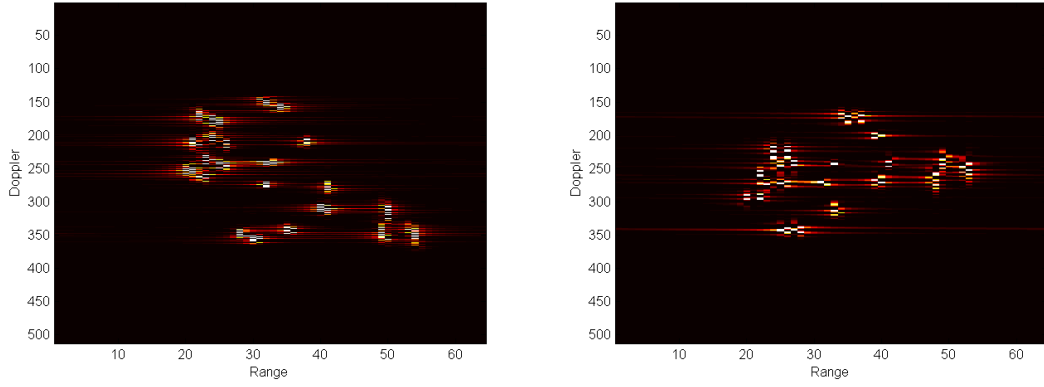


Figure 5.17: Scenario 3: Images reconstructed by STFT using $M/4$ length windows.

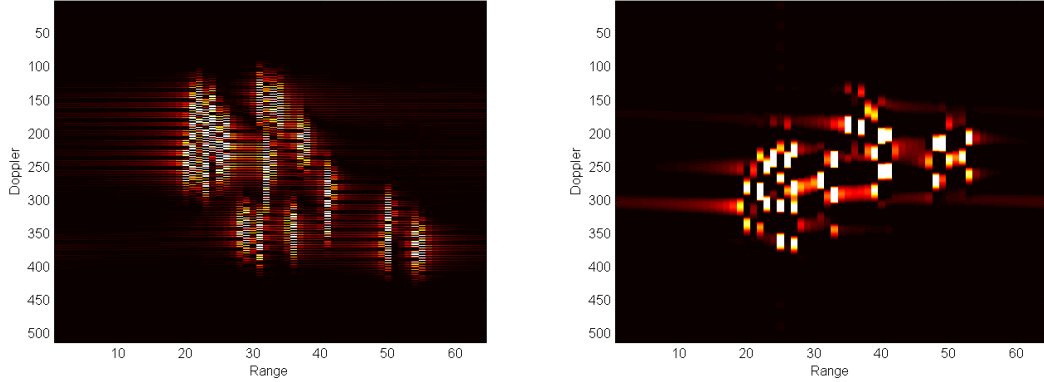


Figure 5.18: Scenario 3: Images reconstructed by STFT using $M/32$ length windows.

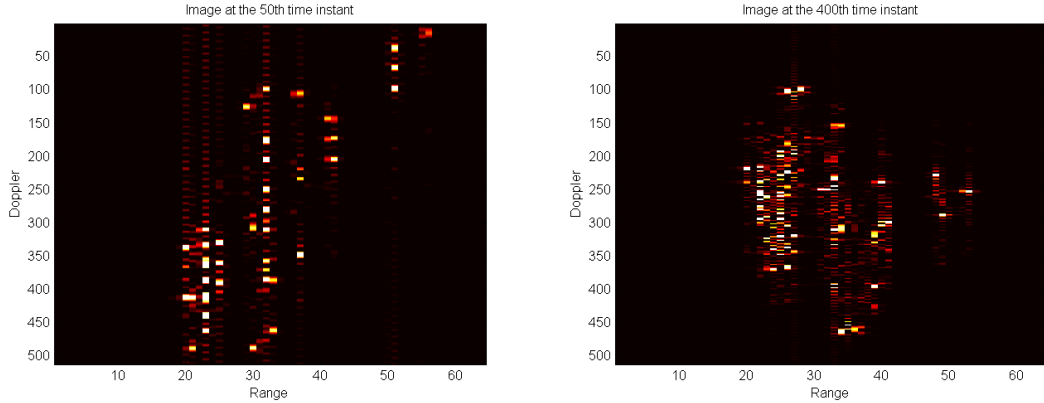


Figure 5.19: Scenario 3: Images reconstructed using Wigner-Ville distribution

Pseudo Wigner-Ville Distribution

Images reconstructed using pseudo Wigner-Ville distribution are shown in Figure 5.20.

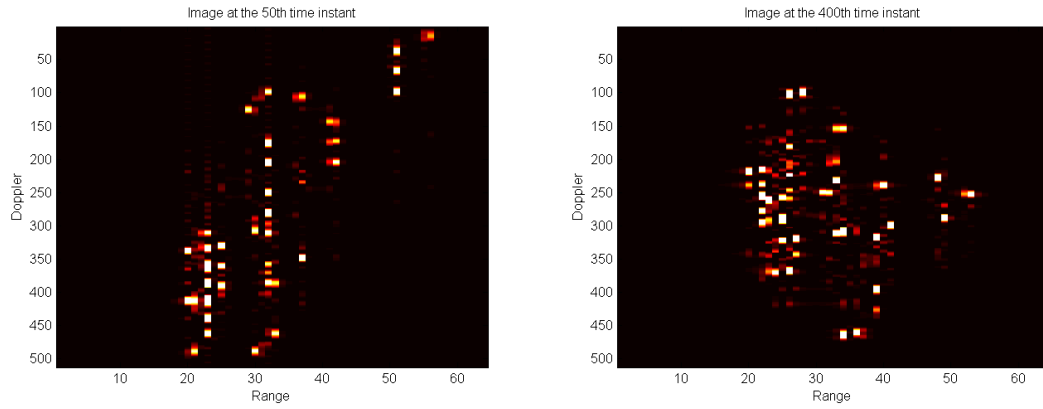


Figure 5.20: Scenario 3: Images reconstructed using pseudo Wigner-Ville distribution

Smoothed Pseudo Wigner-Ville Distribution

Images reconstructed using smoothed pseudo Wigner-Ville distribution are shown in Figure 5.21.

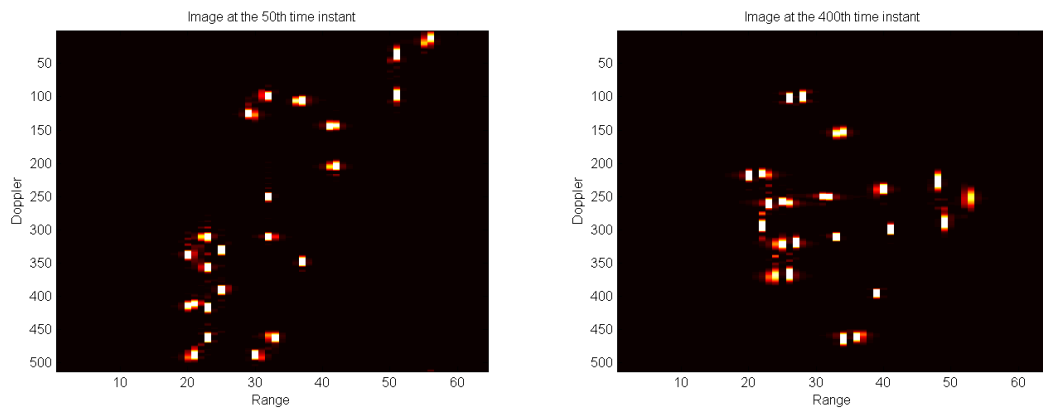


Figure 5.21: Scenario 3: Images reconstructed using smoothed pseudo Wigner-Ville distribution

Choi-Williams Distribution

Images reconstructed using Choi-Williams distribution are shown in Figure 5.22.

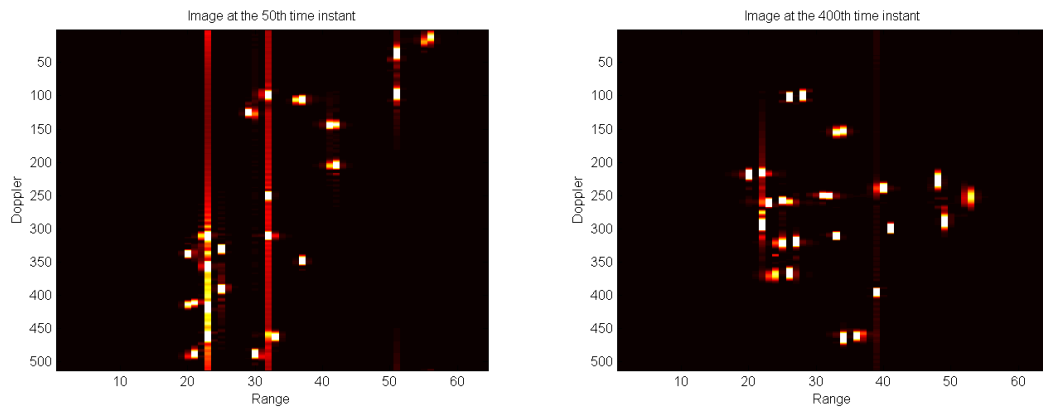


Figure 5.22: Scenario 3: Images reconstructed using Choi-Williams distribution

Born-Jordan Distribution

Images reconstructed using Born-Jordan distribution are shown in Figure 5.23.

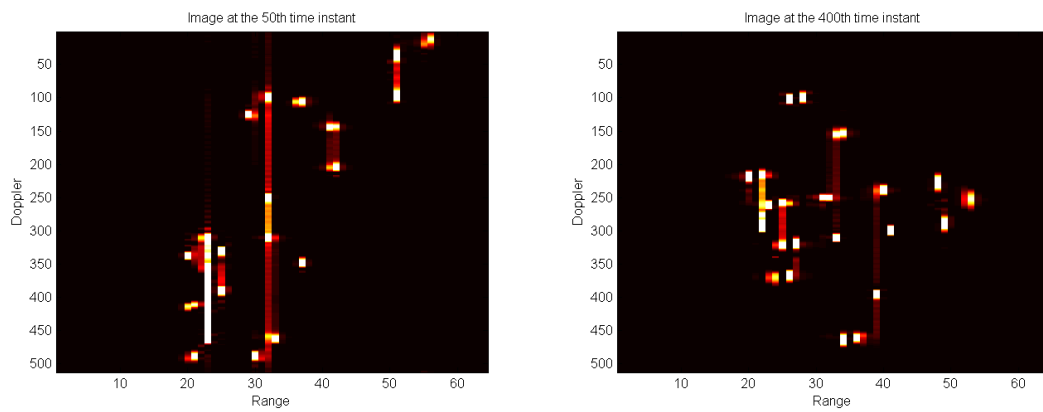


Figure 5.23: Scenario 3: Images reconstructed using Born-Jordan distribution

Zhao-Atlas-Marks Distribution

Images reconstructed using Zhao-Atlas-Marks distribution are shown in Figure 5.24.

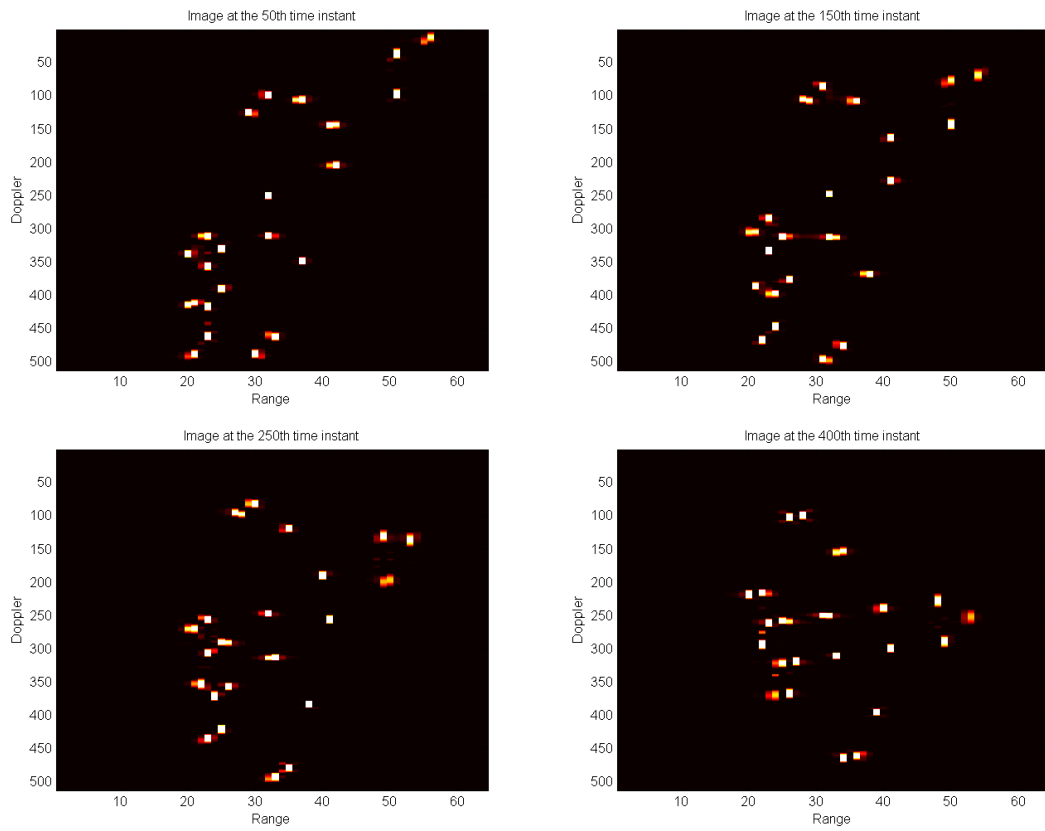


Figure 5.24: Scenario 3: Images reconstructed using Zhao-Atlas-Marks distribution

5.5 Performance Analysis

During this thesis, 5 different simulations are analyzed for various ISAR techniques and obtained reasonable results. Even for the most complex manoeuvring scenario the relative performance of distributions were similar. The best and worst performing distributions were same for all simulations, so that the results were consistent.

It should be noted that there is no performance parameter for comparing the images. However, to be able to observe the scatterers movements and to be able to resolve scatterers from each other is a reasonable performance criteria.

Firstly, it can be clearly observed that even the most basic time-frequency (TF) techniques produce clearer images than conventional Fourier based technique and most of the bi-linear TF transforms performs better than linear TF transforms. It is observed that by selecting proper window size for STFT the images produced for some time instants are clearer than the images obtained by Wigner-Ville and pseudo Wigner-Ville distributions. That is because with larger window good frequency resolution is obtained but then the time-resolution degrades. As seen from the results if small windows are used to achieve time-resolution, the images degrades significantly and even Wigner-Ville distribution becomes much more successful.

Cross-term interference problem explained in Section 4.4 and shown in Equation (4.10) is the key factor that effects the performance of TF distributions. The most successfully distribution is the one to suppress the cross-terms most while keeping the auto-terms disturbed least. Since Wigner-Ville is the one that produces the most cross-term interference terms, it performs the worst among all the bi-linear transforms. The other distributions uses unique smoothed kernels to reduce these cross-terms so that they perform much better compared to Wigner-Ville.

The best performing distributions are Zhao-Atlas-Marks (ZAM) and smoothed pseudo Wigner-Ville (SPWV) distributions for all the 5 simulations. Choi-Williams can also be considered to perform as well but it is observed that as the manoeuvres of the targets gets more complex this distribution fails to suppress the cross-terms (see Figure 5.14 and Figure 5.22) and fails to perform as well as ZAM and SPWV. The ripples explained in subsection 4.4.4 can be clearly seen for Choi-Williams as well as Born-Jordan distributions. It is very reasonable for ZAM and SPWV to perform better compared to others since ZAM is the smoothed version of Born-Jordan distribution along frequency axis and SPWV consists both frequency and time smoothed windows so that these two distributions suppresses the cross-

terms most and becomes the most successful out of all the distributions that are examined.

In fact, theoretically, if perfect motion compensation, re-sampling and polar formatting was applied to all the individual scatterers, the image obtained by conventional Fourier transform would achieve the best result since the scatterers would remain in their range cells during the observation time and the Doppler spectrum would be invariant. However, the time-frequency transforms are chosen to be applied since they have the following advantages over conventional Fourier transform [4]:

- There is no restriction for the individual scatterers to stay in their range cells during the observation time.
- Standard global motion compensation is necessary. There is no need for complicated motion compensation algorithms for individual scatterers.
- The time-frequency transforms can be applied to deblur the image which is still blurred even after complex motion compensation algorithms applied.
- Computational complexity is less.
- Time-varying behaviour of the target can be observed.

CHAPTER 6

CONCLUSIONS AND FUTURE WORK

Inverse Synthetic Aperture Radar is an imaging radar that uses targets rotational motion and performs range-Doppler processing to produce range-Doppler images. In the conventional ISAR system, Fourier transform is used to retrieve Doppler information. However, Fourier transforms are adequate only when the Doppler spectrum of the radar phase history is stationary during the entire observation time. Due the target irregular translational and rotational motion, the Doppler frequencies change over time which results a smeared Doppler spectrum and a blurred image. With the conventional Fourier technique complex motion compensation algorithms such as polar reformatting must be applied to produce clear images. However, resulting ISAR images can be significantly improved by using joint time-frequency transform instead of Fourier transform since this transform can resolve instantaneous Doppler frequencies.

Throughout this thesis, an ISAR simulation in which a target exhibiting yaw, pitch and roll motions (separately or at the same time) is implemented to see the performance of the time-frequency distributions not only for simple rotating targets but also for complex manoeuvring targets. Time-frequency transforms including short-time Fourier transform, Wigner-Ville, pseudo Wigner-Ville, smoothed pseudo Wigner-Ville, Choi-Williams, Born-Jordan and Zhao-Atlas-Marks distributions are examined and compared for both the implemented simulation scenarios but also for the obtained simulated data [3]. As expected, TFFT based image formation performed much better than the conventional Fourier based image formation and bi-linear transforms performed better than the linear transforms. Bi-linear transforms performed better since higher resolutions are achieved both in time and frequency whereas only either one can be achieved in STFT because of uncertainty principle associated with Fourier transform. It is also observed that since the processed signals are multi-component signals and bi-linear time-frequency transforms are quadratic by na-

ture, there corresponds a problem defined as cross-term interference and the performance of time-frequency distributions is directly related to the ability of that transform to suppress the cross-term interference. Thus, best results are obtained by the smoothed pseudo Wigner-Ville and Zhao-Atlas-Mark distributions which can suppress the cross-terms most.

This study showed that time-frequency transforms are the most adequate transforms for imaging even complex manoeuvring targets in ISAR and they have superior resolutions both in time and frequency. TFTs are observed to be excellent for analyzing non-stationary signals. Since the main problem in conventional ISAR is the non-stationary, time-varying Doppler spectrum obtained by Fourier transform, time-frequency transforms are observed to be perfect for ISAR. They are superior to conventional Fourier transform so that high resolution images can be obtained. It is also observed that, no matter how complex the target manoeuvres, smoothed pseudo Wigner-Ville and Zhao-Atlas-Mark distributions achieve the highest resolution and the best image.

The implemented simulation is an important step in designing a more realistic simulation since not only two-dimensional rotation but also three-dimensional rotation of a target is implemented. This simulation can be further developed to simulate more realistic targets by considering the multiple scattering mechanisms, shadowing effects of scatterers to each others and also considering the other assumptions that are made. With the enhanced simulation, more realistic analysis of various ISAR image formation techniques including the ones used in this thesis can be done.

REFERENCES

- [1] Liu Aifang, Zhu Xiaohua, Lu Jinhui, and Liu Zhong. The isar range profile compensation of fast-moving target using the dechirp method. In *Proceedings of the 2003 International Conference on Neural Networks and Signal Processing*, volume 2, pages 1619–1623, December 2003.
- [2] Victor C. Chen and Hao Ling. *Time-Frequency Transforms for Radar Imaging and Signal Analysis*. Artech House, 2002.
- [3] Victor C. Chen. <http://airborne.nrl.navy.mil/vchen/data/>.
- [4] Victor C. Chen. Adaptive time-frequency isar processing. In *Proceedings of SPIE - Volume 2845, Radar Processing, Technology, and Applications*, pages 133–140, November 1996.
- [5] Victor C. Chen. Applications of time-frequency processing to radar imaging. In *Proceedings of SPIE - Volume 2762, Wavelet Applications III*, pages 23–31, March 1996.
- [6] Victor C. Chen. Applications of time-frequency processing to radar imaging. *Optical Engineering - Bellingham - International Society For Optical Engineering*, 36(4):1152–1161, 1997.
- [7] Victor C. Chen. Time-frequency based isar image formation technique. In *Proceedings of SPIE - Volume 3070, Algorithms for Synthetic Aperture Radar Imagery IV*, pages 43–54, July 1997.
- [8] Victor C. Chen. Joint time-frequency transform for radar range-doppler imaging. *IEEE Transactions on Aerospace and Electronic Systems*, 34(2):486–499, April 1998.
- [9] Victor C. Chen. Time-frequency based radar image formation. In *International Conference on Image Processing (ICIP)*, pages 1–4, July 2004.

- [10] Victor C. Chen and Shie Qian. Reconstruction of isar image by time-frequency distribution series. In *URSI International Symposium on Signal, Systems and Electronics ISSSE'95 Proceedings*, pages 251–254, October 1995.
- [11] Victor C. Chen and W.J.Miceli. Time-varying spectral analysis for radar imaging of manoeuvring targets. In *IEE Proceedings - Radar, Sonar and Navigation, Vol. 145*, pages 262–268, October 1998.
- [12] Victor C. Chen and W.J.Miceli. Simulation of isar imaging of moving targets. In *IEE Proceedings - Radar, Sonar and Navigation, Vol. 148*, pages 160–166, June 2001.
- [13] H.I. Choi and W.J. Williams. Improved time-frequency representation of multicomponent signals using exponential kernels. *IEEE Transactions on Acoustics, Speech, and Signal Processing*, 37(6):862–871, 1989.
- [14] Leon Cohen. Generalized phase-space distribution functions. *Journal of Mathematical Physics*, 7(5):781–786, May 1966.
- [15] Leon Cohen. *Time-Frequency Analysis*. Prentice-Hall, 1995.
- [16] F.Berizzi, E.D.Mese, M.Diani, and M.Martorella. High-resolution isar imaging of manoeuvring targets by means of the range instantaneous doppler technique: modeling and performance analysis. *IEEE Transactions on Image Processing*, 10(12):1880–1890, December 2001.
- [17] Wang Genyuan and Bao Zheng. The minimum entropy criterion of range alignment in isar motion compensation. In *Radar 97 (Conf. Publ. No. 449)*, pages 236–239, October 1997.
- [18] G.Gombert and F.Beckner. High resolution 2-d isar image collection and processing. In *Proceedings of the IEEE 1994 National Aerospace and Electronics Conference*, volume 1, pages 371–377, May 1994.
- [19] F. Hlawatsch and G.F. Boudreaux-Bartels. Linear and quadratic time-frequency signal representations. *IEEE Signal Processing Magazine*, 9(2):21–67, 1992.
- [20] Wu Jie and Zhang Yun-hua. A new motion compensation method for isar based on time-frequency analysis and image processing. In *Asia-Pacific Microwave Conference Proceedings*, pages 4–7, December 2005.

- [21] K.Skrapas, G.Boultadakis, A.Karakasiliotis, and P.Frangos. Time-frequency analysis of radar signals for isar applications. In *Proceedings of 2nd International Conference on Recent Advances in Space Technologies*, pages 699–703, June 2005.
- [22] Talip Küçükçılıç. Isar imaging and motion compensation. Master’s thesis, Middle East Technical University, 2006.
- [23] L.C.Trintinalia and Hao Ling. Joint time-frequency isar algorithm for imaging targets with non-point scattering features. In *International Symposium on Signals, Systems, and Electronics, ISSSE '95, Proceedings*, volume 152, pages 247–250, October 1995.
- [24] Fan Luhong, Yiming Pi, and Shunji Huang. Multi-target imaging processing algorithms of isar based on time-frequency analysis. In *International Conference on Radar, CIE '06*, pages 1–4, October 2006.
- [25] Dean L. Mensa. *High-Resolution Radar Cross-Section Imaging*. Artech House, 1991.
- [26] M.Soumekh, S.Nugroho, S.Jones, R.Rysdyk, and S.Tran. Isar imaging of an airborne dc-9 [aircraft]. In *IEEE International Conference on Acoustics, Speech, and Signal Processing*, volume 7, pages 465–468, October 1993.
- [27] M.Xing, R.Wu, and Z.Bao. High resolution isar imaging of high speed moving targets. In *IEE Proceedings - Radar, Sonar and Navigation*, volume 152, pages 58–67, April 2005.
- [28] Shie Qian and Dapang Chen. *Joint Time-Frequency Analysis, Methods and Applications*. Prentice Hall, 1996.
- [29] S.K.Wong, G.Duff, and E.Riseborough. Distortion in the inverse synthetic aperture radar (isar) images of a target with time-varying perturbed motion. In *IEE Proceedings - Radar, Sonar and Navigation*, volume 150, pages 221–227, August 2003.
- [30] S.K.Wong, G.Duff, and E.Riseborough. Distortion in the isar (inverse synthetic aperture radar) images from moving targets. In *International Conference on Image Processing*, volume 1, pages 25–28, October 2004.
- [31] S.Musman, D.Kerr, and C.Bachmann. Automatic recognition of isar ship images. *IEEE Transactions on Aerospace and Electronic Systems*, 32(4):1392–1404, October 1996.

- [32] T. Thayaparan and S. Kennedy. Detection of a manoeuvring air target in sea-clutter using joint time-frequency analysis techniques. In *IEE Proceedings - Radar, Sonar and Navigation, Vol. 151*, pages 19–30, February 2004.
- [33] T. Thayaparan, G. Lampropoulos, S.K. Wong, and E.I. Riseborough. Application of adaptive joint time-frequency algorithm for focusing distorted isar images from simulated and measured radar data. In *IEE Proceedings - Radar, Sonar and Navigation, Vol. 150*, pages 213–220, August 2003.
- [34] T.Sparr. Isar - radar imaging of targets with complicated motion. In *International Conference on Image Processing*, volume 1, pages 5–8, October 2004.
- [35] Ling Wang, Daiyin Zhu, and Zhaoda Zhu. Range alignment in isar motion compensation based on minimum sum. In *CIE '06. International Conference on Radar*, pages 1–4, October 2006.
- [36] Donald R. Wehner. *High-Resolution Radar (2nd Edition)*. Artech House, 1995.
- [37] Y. Zhao, L.E. Atlas, and R.J. Marks. The use of cone-shaped kernels for generalized time-frequency representations of nonstationary signals. *IEEE Transactions on Acoustics, Speech, and Signal Processing*, 38(7):1084–1091, 1990.
- [38] Zhaoda Zhu, Xiaohui Qiu, and Zhishun She. Isar motion compensation using modified doppler centroid tracking method. In *Proceedings of the IEEE 1996 National Aerospace and Electronics Conference, Vol. 1*, pages 359–363, May 1996.
- [39] Zhaoda Zhu and Zhishun She. Isar motion compensation and superresolution imaging of aircraft. In *Proceedings of the IEEE 1992 National Aerospace and Electronics Conference, Vol. 1*, pages 291–296, May 1992.
- [40] Zhaoda Zhu and Zhishun She. Motion compensation of isar in frequency domain. In *Proceedings of the IEEE 1993 National Aerospace and Electronics Conference, Vol. 1*, pages 299–302, May 1993.